



# Supramolecular Tessellations by a Rigid Naphthalene Diimide Triangle

Yassine Beldjoudi,<sup>†</sup> Ashwin Narayanan,<sup>‡</sup> Indranil Roy,<sup>†</sup> Tyler J. Pearson,<sup>†</sup> M. Mustafa Cetin,<sup>†</sup> Minh T. Nguyen,<sup>†</sup> Matthew D. Krzyaniak,<sup>†,||</sup> Fehaid M. Alsubaie,<sup>¥</sup> Michael R. Wasielewski,<sup>†,||</sup> Samuel I. Stupp,<sup>†,‡,£,⊥</sup> and J. Fraser Stoddart<sup>†,#,§\*</sup>

<sup>†</sup>Department of Chemistry, <sup>‡</sup>Department of Materials Science and Engineering, <sup>§</sup>Institute for Sustainability and Energy, <sup>£</sup>Department of Biomedical Engineering, Northwestern University, Evanston, Illinois 60208, United States.

<sup>||</sup>Department of Medicine and Simpson-Querrey Institute for BioNanotechnology, Northwestern University, Chicago, Illinois 60611, United States.

<sup>¥</sup>Joint Center of Excellence in Integrated Nanosystems, King Abdulaziz City for Science and Technology, Riyadh 11442, Kingdom of Saudi Arabia.

<sup>#</sup>Institute for Molecular Design and Synthesis, Tianjin University, 92 Weijin Road, Nankai District, Tianjin 300072, China.

<sup>§</sup>School of Chemistry, University of New South Wales, Sydney, NSW 2052, Australia.

### **\*Correspondence Address**

Professor J. Fraser Stoddart  
Department of Chemistry  
Northwestern University  
2145 Sheridan Road  
Evanston, IL 60208 (USA)  
Tel: (+1)-847-491-3793  
Email: [stoddart@northwestern.edu](mailto:stoddart@northwestern.edu)

## ■ ABSTRACT

Tessellation of organic polygons through  $[\pi\cdots\pi]$  and charge-transfer (CT) interactions offers a unique opportunity to construct supramolecular organic electronic materials with 2D topologies. Our approach of exploring the 3D topology of 2D tessellations of a naphthalene diimide-based molecular triangle (**NDI-Δ**) reveals that the 2D molecular arrangement is sensitive to the identity of the solvent and solute concentrations. Utilization of non-halogenated solvents, combined with careful tailoring of the concentrations, results in **NDI-Δ** self-assembling through  $[\pi\cdots\pi]$  interactions into 2D honeycomb triangular and hexagonal tiling patterns. Co-crystallization of **NDI-Δ** with tetrathiafulvalene (**TTF**) leads systematically to the formation of 2D tessellations as a result of superstructure directing of CT interactions. Different solvents lead to different packing arrangements. Using MeCN,  $\text{CHCl}_3$  and  $\text{CH}_2\text{Cl}_2$ , we identified three sets of co-crystals, namely **CT-A**, **CT-B**, and **CT-C** respectively. Solvent modulation plays a critical role in controlling, not only the **NDI-Δ:TTF** stoichiometric ratios and the molecular arrangements in the crystal superstructures, but also prevents the inclusion of **TTF** guests inside the cavities of **NDI-Δ**. Confinement of **TTF** inside the **NDI-Δ** cavities in the **CT-A** superstructure enhances the CT character with the observation of a broad absorption band in the NIR region. In the **CT-B** superstructure, the  $\text{CHCl}_3$  lattice molecules establish a set of  $[\text{Cl}\cdots\text{Cl}]$  and  $[\text{Cl}\cdots\text{S}]$  intermolecular interactions, leading to the formation of a hexagonal grid of solvent in which **NDI-Δ** forms a triangular grid. In the **CT-C** superstructure, three **TTF** molecules self-assemble, forming a supramolecular isosceles, triangle **TTF-Δ**, which tiles in a plane alongside the **NDI-Δ**, producing a 3+3 honeycomb tiling pattern of the two different polygons. Solid-state spectroscopic investigations on **CT-C**, revealed the existence of an absorption band at 2500 nm which, on the basis of TDDFT calculations was attributed to the mixed-valence character between two **TTF**<sup>+</sup> and one neutral **TTF** molecule.

## ■ INTRODUCTION

Tessellation or tiling is a process of arranging polygons in a plane in order to cover a surface entirely without gaps or overlaps, and in so doing, generate uniform or irregular two-dimensional (2D) patterns. Tessellation has been used<sup>1</sup> to tile regular polygons for decoration in art since antiquity. The mathematical treatment of tiling regular polygons, however, was first reported in 1619 by Kepler,<sup>2</sup> who identified 11 types of Archimedean tilings. At the molecular level, a growing interest has emerged in the past decades in 2D tiling of semi-regular Archimedean Tilings<sup>3</sup> (ATs) and quasi-crystalline superstructures<sup>4</sup> (QCs) on account of their potential optical,<sup>5</sup> magnetic<sup>6</sup> and catalytic<sup>7</sup> properties. Molecular tiling, such as the programmed self-assembly of DNA molecules,<sup>8</sup> liquid-crystal engineering,<sup>9</sup> binary nanoparticle superlattices<sup>10</sup> and polymeric systems<sup>11</sup> have all been reported in the recent years.

Tessellations with shape-persistent polygons, leading to the construction of 2D networks, is less well explored because of synthetic difficulties in accessing such macrocyclic structures. Triangular systems, decorated with long alkyl chains, have been employed<sup>12</sup> in the construction of 2D glassy-state networks. Other studies<sup>13</sup> have demonstrated the emergence of chiral multicomponent supramolecular networks formed by achiral molecules at the interfaces with chiral solvents and achiral substrates. A more recent investigation has led<sup>14</sup> to the report of the tiling of hexagonal macrocycles of different sizes through a combination of van der Waals (VDW) interactions and hydrogen bonding to form periodically ordered hexagonal 2D networks at liquid-solid interfaces. Furthermore, macrocyclic polygons of triangular or square-shaped molecular structures have been tessellated<sup>15</sup> in a 2D network using covalent bonds with additional linkers to generate 2D multiporous networks. Also, molecular tessellations, using organic macrocyclic polygons fabricated on a metal surface, have been observed with a combination of scanning tunneling

microscopy, synchrotron radiation photoelectron spectroscopic and X-ray spectroscopic techniques. Detailed 3D superstructural information derived from the X-ray crystallographic studies of tessellated materials, however, is still a little explored topic. Recently, X-ray crystallography has been utilized<sup>16</sup> to elucidate the 3D supramolecular architectures of isomeric 2,5- and 2,6-bis(iodoethynyl)pyrazine which assemble to generate polygonal tessellations and intertwined double helices as the result of intermolecular ethynyl [C—I···N] halogen bonding. Investigations of the 3D supramolecular architectures using X-ray crystallography to characterize the superstructure of tessellated organic macrocyclic polygons in 2D networks, however, remain unexplored to the best of our knowledge.

Since the discovery of the metallic conductivity at ambient temperature<sup>17</sup> in a **TCNQ:TTF** (tetracyanoquinodimethane:tetrathiafulvalene) charge-transfer (CT) complex in the early 1970s, followed by the observation of its superconductivity at low temperature<sup>18</sup> in 2004, much effort has been focused<sup>19</sup> on the design (Figure 1a) of 1D  $\pi$ -conjugated organic materials with desirable electronic properties. The **TCNQ:TTF** CT complex consists of infinite segregated  $\pi$ -stacks of donors (**D**) and acceptors (**A**). Mixed-stack CT assemblies, composed of (Figure 1b) alternating **D** and **A** aromatic molecules, provide<sup>18</sup> the inherent and uniform doping required to obtain excellent conducting properties. Under external stimuli, such as pressure, temperature or light, electrons delocalized along the **D/A** stack leading<sup>20</sup> to the formation of fractional charges (ionic phase) and increase conductivity. In addition, the structural synergy between a hydrogen-bonded network and the CT complexation of **D** and **A** molecules in mixed-stack CT superstructures has led to the emergence of ferroelectric behavior at room temperature.<sup>21</sup> On the other hand, 2D semi-conductive materials, such as graphene<sup>22</sup>, boron nitride<sup>23</sup> and transition metal dichalcogenides<sup>24</sup>, are based on covalently interconnected atoms to form honeycomb 2D network patterns, and are widely utilized

in energy harvesting technologies<sup>25</sup> and flexible electronics.<sup>26</sup>

In the past two decades, 1,4,5,8-naphthalene tetracarboxylic diimides (NDI) have emerged as an important class of functional  $\pi$ -systems, often finding application in organic electronics,<sup>27</sup> photovoltaic devices,<sup>28</sup> and sensors.<sup>29</sup> Recently, this molecular motif has also been considered as a potential lithium-ion electrode material, owing to its low molecular weight, high electron affinity and high charge carrier mobility.<sup>27a,30</sup> More recently, we have investigated<sup>31,32</sup> the structural and electronic properties of rigid shape-persistent NDI triangles (**NDI- $\Delta$** ) (Figure 2a) which display (i) electron sharing between three NDI units, leading to the observation of stepwise six-electron reductions<sup>31</sup>, and (ii) anionic recognition properties.<sup>32</sup> Awaga et al.<sup>33</sup> have reported the superstructure of the monoradical of **NDI- $\Delta$** <sup>•-</sup> which crystallizes in a K<sub>4</sub> structure; band-structure calculations suggest a metallic ground state, Dirac cones, and flat bands characteristic of the superstructure. The material, however, was found experimentally to be weakly semiconductive. More recent studies<sup>34</sup> have shown that the tris-radical [(+)-**NDI- $\Delta$** <sup>3</sup>(<sup>•-</sup>)(CoCp<sup>2+</sup>)<sub>3</sub>] complex has a spin-frustrated doublet ground state and a thermally accessible quartet state. In addition, at low temperature, it exhibits<sup>34</sup> ferromagnetic ordering with a Curie temperature  $T_c$  of 20 K. In this context, there is a combination of four parameters to be considered, namely (i) the rigid structure and the triangular shape of **NDI- $\Delta$**  which can adopt different 2D tessellation packing motifs following the AT tiling principles, (ii) the confinement of electron donors inside the cavities leading to the formation of host-guest complexes which can facilitate CT, (iii) the greater electron-deficiency of **NDI- $\Delta$** , compared to that of the NDI monomer, enhances the macrocycles electron affinity, and (iv) the intramolecular electron sharing between the three NDI units of **NDI- $\Delta$**  which offer potentially additional degrees of freedom for charge transport in 2D or 3D in tessellated packing patterns.

In the present work, we report the tessellations (Figure 2b) of a shape-persistent regular polygon **NDI-Δ** in a 2D framework through favorable  $[\pi \cdots \pi]$  interactions between the NDI units. Furthermore, because the triangle is the smallest geometry capable of achieving regular and semi-regular tiling, several tiling patterns, such as triangular and hexagonal tiling have been achieved through solvent and solute concentration modulations. Indeed, careful modulation of the solvent composition (halogenated versus non-halogenated solvents) and solute concentrations induce a dramatic change in the arrangement of **NDI-Δ** in crystal superstructures. In addition, we report that utilization of tetrathiafulvalene (**TTF**) as an electron donor can offer systematic in-plane 2D networks (Figure 2c) of CT interactions since propagation of CT interactions are superstructure directing. Molecular packing in the crystal superstructure and the formation of host-guest supramolecular complexation between **NDI-Δ** and **TTF**, however, can be controlled through solvent modulation. Detailed information of the 3D arrangement of **NDI-Δ** polygons and **TTF** have been investigated thoroughly using X-ray crystallography. In addition, detail analysis of the molecular structures has provided valuable information on the valency of the different components and the dominant intermolecular interactions ( $[\text{Cl} \cdots \pi]$ ,  $[\pi \cdots \pi]$ , CT interactions etc.) which influence the molecular arrangements. The physical properties have been unraveled using a combination of spectroscopic, magnetic, and electron-transport measurements in addition to theoretical calculations.

## ■ RESULTS AND DISCUSSION

### Crystal Engineering of the **NDI-Δ** and **NDI-Δ•TTF** Cocrystals

*a. Tessellation of **NDI-Δ** through  $[\pi \cdots \pi]$  interactions:* The synthesis of **NDI-Δ** was carried out

according to standard literature procedures.<sup>31,32</sup> Crystal engineering of **NDI-Δ** in a 2D network requires understanding the different forces that can enhance or prevent the formation of superstructural patterns. The crystal packing of **NDI-Δ** is very sensitive to the solvent identity and solute concentrations. Crystallization processes utilized for the growth of the different **NDI-Δ** superstructures are summarized in Figure 3. The superstructure of **NDI-Δ** crystallized from CH<sub>2</sub>Cl<sub>2</sub> has been already reported,<sup>32</sup> and presents many voids as a result of the removal of the solvent electron density during refinement of the crystal superstructure. For a better understanding of the role of solvent molecules in the packing of **NDI-Δ**, we crystallized **NDI-Δ** from CH<sub>2</sub>Cl<sub>2</sub> at a concentration of  $5.7 \times 10^{-4}$  M. **NDI-Δ** in CH<sub>2</sub>Cl<sub>2</sub> crystallizes in the cubic *I*2/3 space group, similar to that reported<sup>32</sup> in the literature (Figure S1). The current crystal superstructure, however, reveals (Figure S1a) the presence of three disordered CH<sub>2</sub>Cl<sub>2</sub> molecules and two NDI units in the asymmetric unit. This superstructure displays the existence of [C-H…Cl] and [Cl…π(NDI)] interactions which prevent [π…π] interactions between these NDI units. In order to confirm the competition between the [Cl…π(NDI)] and [π…π] interactions, we crystallized **NDI-Δ** from a CHCl<sub>3</sub> solution. Once again, the NDI units do not interact as a result of [π…π] interactions, but rather establish (Figure S2) a set of [Cl…π(NDI)] and [Cl…H(cyclohexane)] interactions. Furthermore, CHCl<sub>3</sub> molecules occupy the **NDI-Δ** cavity and interact on account of [Cl…π] interactions (Figure S2b). Previous studies revealed<sup>35</sup> the role of lone pair…π interactions, which take place between lone pair-bearing atoms in neutral molecules and electron-deficient π-acidic aromatic systems in Z-DNA, for example. Other studies have revealed<sup>36</sup> that NDIs are electron-deficient molecules and have a strong tendency to interact with electron-rich lone pair-bearing atoms. Crystallization of **NDI-Δ** in 1,2-dihalogenated ethane or ethene solvents has revealed<sup>37</sup> the absence of the [π…π] interactions between the NDI units. Clearly, halogenated solvents (CH<sub>2</sub>Cl<sub>2</sub>,

$\text{CHCl}_3$ ) (Figure S1,S2) establish a network of  $[\text{Cl}\cdots\text{H}(\text{cyclohexane})]$  and  $[\text{Cl}\cdots\pi(\text{NDI})]$  interactions which prevent in-plane packing of **NDI-Δ** through  $[\pi\cdots\pi]$  interactions. In this context, utilization of non-halogenated and relatively low-solubilizing solvents, such as MeCN, is essential in order to enhance the self-assembly of **NDI-Δ** through  $[\pi\cdots\pi]$  interactions which generate in-plane 2D **NDI-Δ** tiling patterns. Notably, crystallization of **NDI-Δ** from MeCN has been proven to be concentration dependent; the crystal growth procedures are summarized in Figure 3. Three different polymorphs, named **α-NDI-Δ**, **β-NDI-Δ** and **γ-NDI-Δ**, have been identified by employing different solute concentrations. While **α-NDI-Δ** crystallizes at the highest concentration ( $5 \times 10^{-3}$  M) of **NDI-Δ**, **β-NDI-Δ** and **γ-NDI-Δ** crystallize at  $5 \times 10^{-4}$  and  $9.6 \times 10^{-5}$  M, respectively. Seemingly, the **β-NDI-Δ** and **γ-NDI-Δ** phases are thermodynamically favored, while fast crystallization of **NDI-Δ** offers selectively the **α-NDI-Δ** phase as a kinetic polymorph. According to the density rule,<sup>38</sup> superstructures with higher density (more efficient packing) tend to have greater (enthalpic) stability. In this context, the  $\gamma$ -polymorph ( $d = 1.71 \text{ g/mm}^3$ ) is enthalpically more favorable than the  $\beta$ -**NDI-Δ** ( $d = 1.42 \text{ g/mm}^3$ ) and  $\alpha$ -**NDI-Δ** ( $d = 1.37 \text{ g/mm}^3$ ). Recent investigations on the tiling of hexagonal macrocycles into 2D hexagonal network have been shown<sup>14</sup> to be concentration dependent. To the best of our knowledge, there has been no systematic investigations of the effects of solvent identity and concentration on the packing geometries of triangular macrocycles.

**b. Tessellation of NDI-Δ and TTF through CT interactions:** Co-crystallization of the electron-deficient **NDI-Δ** with electron-rich **TTF** at a molar ratio of 1 : 3 leads (Figure 4) to the formation of three sets of CT complexes—named as the **CT-A**, **CT-B** and **CT-C** complexes—depending on the crystallization conditions. Crystallization by slow evaporation of MeCN yields selectively the **CT-A** complex with a molar ratio 2 : 5 **NDI-Δ:TTF** in the resulting crystal structure. Notably,

**CT-A** shows the formation of an host-guest complex between two **NDI-Δ** units and one **TTF** molecule. Slow diffusion of hexane into a solution of **NDI-Δ** in  $\text{CHCl}_3$  and  $\text{CH}_2\text{Cl}_2$  leads to the formation of two different complexes, namely **CT-B** and **CT-C**, with **NDI-Δ:TTF** molar ratios in the crystal superstructures of 2 : 3 and 1 : 3, respectively. Neither of the **CT-B** and **CT-C** superstructures display the presence of **TTF** inside the **NDI-Δ** cavity because of the stronger affinity of the solvent molecules for that cavity (*vide infra*). All three superstructures display 2D-tiling patterns composed of **NDI-Δ** and **TTF**, indicating that the CT interactions between the **TTF** and **NDI** units are more favored than are the  $[\text{Cl}\cdots\pi(\text{NDI})]$  interactions.

### Crystallographic Studies of the **NDI-Δ** Structures

All the crystallographic data for superstructures **NDI-Δ•CH<sub>2</sub>Cl<sub>2</sub>** and **NDI-Δ•CHCl<sub>3</sub>** are presented in the Supplementary Information, while the crystallographic information for the three polymorphs **α-NDI-Δ**, **β-NDI-Δ** and **γ-NDI-Δ** are discussed below.

**a. Structure α-NDI-Δ:** At high concentration of the **NDI-Δ** in MeCN ( $5 \times 10^{-3}$  M), **α-NDI-Δ** crystallizes (Figure 5a) in the monoclinic  $P2_1$  space group with two **NDI-Δ** molecules in the asymmetric unit. These two molecules form a supramolecular dimer as a result of  $[\pi\cdots\pi]$  interactions at a distance of 3.52 Å between two NDI units of each crystallographically distinct **NDI-Δ**, with a deviation from a parallel face-to-face interaction of  $\sim 72^\circ$ . One of the two **NDI-Δ** units contains one molecule of Et<sub>2</sub>O in its cavity, while the second **NDI-Δ** contains a MeCN molecule inside its cavity (Figure S3a). This behavior could be related to the low solubility of the **NDI-Δ** in MeCN which leads to fast crystallization of **NDI-Δ** at high concentrations in a MeCN/Et<sub>2</sub>O solvent mixture. Along the *a*-axis and *b*-axis, each molecule of the asymmetric unit establishes  $[\text{C-H}\cdots\text{O}]$  interactions (mean 3.1 Å,  $\theta_{[\text{C-H}\cdots\text{O}]} = 137^\circ$ ) with two symmetrically related

neighboring molecules, forming (Figure 5b, Figure S3b,c) zig-zag chains of **NDI-Δ**. Notably, **α-NDI-Δ** does not form supramolecular triangular nanotubes, as observed in the case of **β-NDI-Δ** and **γ-NDI-Δ** (*vide infra*) or when 1,2-dihaloethane and -ethene ( $\text{BrCH}_2\text{CH}_2\text{Br}$ ,  $\text{ClCH}_2\text{CH}_2\text{Br}$ , and  $\text{ClCH}_2\text{CH}_2\text{I}$ ) are utilized for crystallization<sup>37</sup> (Figure S3d,e). Seemingly, the existence of structure-directing interactions (halogen···halogen bonding) between the solvent molecules residing inside the cavity of **NDI-Δ** are structure-directing toward the formation of tubular superstructures.

**b. Structure  $\beta$ -NDI-Δ.** In an attempt to decrease the nucleation kinetics, we diluted a solution of **NDI-Δ** in MeCN ( $5 \times 10^{-4}$  M). Slow diffusion of  $\text{Et}_2\text{O}$  into the solution resulted in colorless needles suitable for crystallographic studies. **β-NDI-Δ** crystallizes in the triclinic *P1* space group with two molecules in the asymmetric unit; each triangle contains (Figure 6a) one molecule of  $\text{Et}_2\text{O}$ . This dimeric superstructure interacts through  $[\pi \cdots \pi]$  interactions between NDI units with a deviation from a parallel face-to-face interaction of 11.8 (2)°. The **NDI-Δ** units stack in a parallel manner to form (Figure 6b) triangular supramolecular nanotubes. The stacking of **NDI-Δ** via hydrogen bonding to form a nanotubular structure with a perpendicular rotation angle of 60° has been reported<sup>37</sup> in the literature for the case where 1,2-dihaloethane or -ethene ( $\text{BrCH}_2\text{CH}_2\text{Br}$ ,  $\text{ClCH}_2\text{CH}_2\text{Br}$ , and  $\text{ClCH}_2\text{CH}_2\text{I}$ ) are present in the cavity of **NDI-Δ**. Remarkably, in the **β-NDI-Δ** structure, all the polygon faces interact via face-to-face  $[\pi \cdots \pi]$  interactions in the range of 3.34 to 3.46 Å between the NDI units; these interactions propagate (Figure 6c) in the *bc*-plane to form a distorted hexagonal superstructure (six triangles around a vertex, 121212). In the ATs, the structure of **β-NDI-Δ** can be considered<sup>1</sup> (Figure 6d,e) as a truncated 2D honeycomb triangular tiling of *P6m* Euclidean plane symmetry. Tiling of shape-persistent molecular triangles on a metal surface has been achieved<sup>12</sup> through dispersive forces between long alkyl chains, leading to the formation of a 2D network. More recently, covalent 2D tiling of *C<sub>3</sub>* and *C<sub>6</sub>* symmetric molecular polygons via the

Schiff base reaction has been reported.<sup>39</sup> Tessellation of shape-persistent molecular polygons through  $[\pi \cdots \pi]$  interactions between polycyclic aromatic hydrocarbons, however, has not yet been reported: this line of research is of interest because the optical and electronic properties of numerous organic materials arise from the propagation of such interactions.<sup>40</sup>

**c. Structure  $\gamma$ -NDI- $\Delta$ :** Further dilution of the **NDI- $\Delta$**  in MeCN ( $9.6 \times 10^{-5}$  M) and crystallization by the slow diffusion of Et<sub>2</sub>O resulted in colorless hexagonal needles suitable for single-crystal crystallography.  **$\gamma$ -NDI- $\Delta$**  crystallizes in the hexagonal *P*6<sub>2</sub> space group with one **NDI- $\Delta$**  in the asymmetric unit. The cavity of **NDI- $\Delta$**  contains (Figure 7a,b, Figure S4a) one molecule of Et<sub>2</sub>O. While along the *c*-axis, the **NDI- $\Delta$**  establishes a set of [C=O $\cdots$  H] hydrogen bonds to form supramolecular nanotubes (Figure S4b) similar to those found in  **$\beta$ -NDI- $\Delta$** , in the *ab*-plane **NDI- $\Delta$**  interacts via  $[\pi \cdots \pi]$  interactions of  $\sim 3.4$  Å between the NDI units to form (Figure 7a,b) a uniform hexagonal superstructure, *hex*-**NDI- $\Delta$** . In this case, six **NDI- $\Delta$**  molecules around a vertex form a small cavity of 8.2 Å diameter (Figure 7a) and these *hex*-**NDI- $\Delta$** , when viewed along the *a*-axis, together form (Figure S4e) a boat-like superstructure. In ATs, the *hex*-**NDI- $\Delta$**  superstructure is characterized by *P*6<sub>3</sub> symmetry. The arrangement of these *hex*-**NDI- $\Delta$**  in the crystal structure is different from the arrangement of the **NDI- $\Delta$**  units in  **$\beta$ -NDI- $\Delta$** . The ATs in  **$\gamma$ -NDI- $\Delta$**  are considered as a case of periodic isogonal tiling<sup>1</sup> by non-edge-to-edge convex regular *hex*-**NDI- $\Delta$**  polygons (Figure 7c). These *hex*-**NDI- $\Delta$**  are surrounded by MeCN solvent molecules which form (Figure S4c,d) a hexagonal grid of *P*6<sub>3</sub> symmetry in the ATs. Although the hexagonal tiling of hexagonal polygons was reported<sup>14</sup> recently, to the best of our knowledge, hexagonal molecular tiling of triangular polygons remains elusive. The present results provide useful insight into the control of packing of regular polygons through careful selection of the solvent (halogenated versus non-

halogenated) as well as the choice of the concentration of the solute in non-halogenated solvents.

### Crystallographic Studies of the CT Complexes

Three sets of co-crystals of **NDI-Δ**•**TTF** have been obtained using different crystallization conditions. Solvent modulation plays a critical role in controlling, not only the D/A stoichiometry ratio and the molecular arrangement in the crystal structure, but also it prevents the inclusion of the guest **TTF** inside the cavity of the **NDI-Δ** macrocycle. All the crystallographic data are reported in Table 2.

**Crystal structure of CT-A:** **CT-A** adopts (Figure 8a, Figure S5a) the triclinic space group  $P\bar{1}$  with one **NDI-Δ** molecule and 2.5 **TTF** molecules in the asymmetric unit. Two **NDI-Δ** molecules ( $(\text{NDI-}\Delta)_2$ ) exhibit the classical  $C_3$  rotation ( $60^\circ$ ) of hydrogen-bonded **NDI-Δ** ( $[\text{C-H}\cdots\text{O}]$  interactions (mean  $d_{[\text{C}\cdots\text{O}]} = 3.39 \text{ \AA}$ ; mean  $\theta_{[\text{C-H}\cdots\text{O}]} = 159^\circ$ ) to form (Figure 8b) a cavity  $\sim 12 \text{ \AA}$  in length. The structure, however, does not form a long-range tubular superstructure because of the weak directionality of the C–H interactions between **TTF** molecules inside the **NDI-Δ** cavity. The cavity of the  $(\text{NDI-}\Delta)_2$  dimer encapsulates one **TTF** molecule (**TTF-1**) which is disordered between the two **NDI-Δ** molecules with an occupancy factor of 0.5. Variable-temperature powder-XRD measurements revealed (Figure S12) no change in the powder pattern profile, indicating that the disorder of **TTF-1** is rather static.  $^1\text{H}$  NMR Titration of **TTF** into a solution of **NDI-Δ** in MeCN revealed (Figure S15) an upfield shift of the NDI aromatic protons: a fit of the chemical shifts using a 1:1 binding model for a host-guest complex gave a binding constant of  $1.8 \pm 0.02 \text{ M}^{-1}$ . The guest **TTF-1** molecule is in close contact with the three NDI units of **NDI-Δ**, establishing (Figure 8a) a set of face-to-face  $[\pi\cdots\pi]$  interactions of  $\sim 3.3 \text{ \AA}$  and edge-to-face  $[\text{S}\cdots\pi(\text{NDI})]$  interactions of 2.95 and  $3.00 \text{ \AA}$ . These interactions are below the van der Waals radii for  $[\text{C}\cdots\text{C}]$  and  $[\text{S}\cdots\text{C}]$

distances of 3.4 Å and 3.5 Å, respectively. One of the edges of the **NDI-Δ** molecule interacts via  $[\pi\cdots\pi]$  interactions of 3.35 Å between the NDI units to form a dimeric superstructure. The two other edges interact in a face-to-face fashion with two other **TTF** molecules, named **TTF-2** and **TTF-3** (Figure S5a). These two **TTF** molecules are distant from the NDI units at 3.5 Å. The relative orientation the **TTF** molecules with respect to the plane of the NDI units, however, is different. While **TTF-1** and **TTF-2** are oriented perpendicularly to the NDI units' plane, **TTF-3** is oriented parallel to the NDI unit plane (Figure 8a and Figure S5a). The **NDI-Δ** and **TTF** molecules forms a 2D network of CT interactions in the *bc*-plane (Figure 8c, Figure S5b,c). These layers are interconnected by means of a set of  $[\pi\cdots\pi]$  interactions between the NDI units and  $[\text{S}\cdots\text{S}]$  interactions between the **TTF** molecules ( $d_{\text{S-S}}$  in a range 2.98 to 3.70 Å; VDW radii for  $[\text{S}\cdots\text{S}]$  interaction is 3.6 Å) (Figure S5d).

In previous studies<sup>41</sup> on CT complexes, the valency of organic molecules, as well as the electron transporting properties of the materials, can be predicted by analyzing the details of their superstructures, such as bond lengths, bond angles, separation distances and the packing motifs of donor and acceptor species. The side view reveals (Figure 8a), that both **TTF-1** and **TTF-3** molecules are near planar (3.3 and 4.4°, respectively) while **TTF-2** is slightly curved along the dithiole and lies with a torsion angle of ~11.3°. Such distortion could be a result of weak attractive intermolecular interactions. DFT calculations reveal that the structure of an isolated **TTF** molecule in the gas phase is not planar. Instead, it adopts a 'boat-like' conformation with a  $C_{2v}$  point group<sup>42</sup> where the two pentagonal rings are slightly bent with an angle of about 12.9° and a C=C bond length of 1.33 Å. Additionally, the C=C bond lengths are benchmarks for predicting the oxidation states of TTF species.<sup>42</sup> Because they are adjacent to NDI units, the **TTF** molecules were expected to possess positive charges, and the central C=C bond was expected to be elongated by the single-

bond component from the resonance structure compared with that in the neutral **TTF**. **TTF-1** and **TTF-2** are both thermally disordered preventing detailed analysis of the C=C bond lengths. The average of the C=C bond length, however, is estimated to be of 1.49 and 1.43 Å for **TTF-1** and **TTF-2**, respectively, whilst in **TTF-3**, the C=C bond length is only slightly elongated to 1.36 Å. The C=C bond length in **TCNQ-TTF** is 1.369 Å ( $\rho_{TTF} = +0.59$ ).<sup>43</sup> DFT calculations reveal<sup>43</sup> that radical **TTF<sup>+</sup>** is characterized by a C=C bond length of 1.396 Å, while in **TTF<sup>2+</sup>**, the bond length is 1.454 Å. In this context, it is obvious that **TTF-1** and **TTF-2** are in their radical cationic states, while **TTF-3** is only partially oxidized owing to a CT to the electron-poor **NDI-Δ** at 100 K. It has been previously reported<sup>44</sup> that confinement of **TTF** inside metal-organic framework (MOF) pores induce an enhancement of a CT and a significant increase in the conductivity. EPR investigations of **CT-A** in the solid-state revealed the existence of an anisotropic signal. Simulated results indicate (Figure S25) the existence of two types of paramagnetic centers, with a main component of  $g_{iso} = 2.0079$  and a minor component with  $g_{iso} = 2.004$ . The EPR spectrum of the *ref*-**NDI-TTF** composite offered (Figure S28) a very weak isotropic signal, indicative of a weak CT. Previous studies revealed that the EPR signal of **TTF**, either in solution or in the solid state, is centered at around  $g = 2.006$ .<sup>45</sup> The g-tensor of the **NDI-Δ<sup>-</sup>** and **NDI-Δ<sup>3-</sup>** have been reported<sup>33,34</sup> to be centered at  $\sim g_{iso} = 2.0035$ . Therefore, the slight shift of the  $g_{iso}$ -value is indicative of both (i) the delocalization of the spin density as the result of the close intermolecular contacts and (ii) the contribution to the anisotropic shape of the EPR signal from chemically and crystallographically distinct paramagnetic components. Although the magnetic susceptibility (Figure S29) in the high-temperature region indicates the analogous paramagnetism arising from the spin-1/2 residing on each **D<sup>+</sup>** and **A<sup>-</sup>** radical, its monotonic increase on cooling combined with the field dependence of the magnetisation at low temperatures (Figure S31) represent the absence of the spin Peierls transition. The  $\chi T$  product

in Figure S30 is lower than the expected value for a  $S = \frac{1}{2}$  system which denotes either a partial charge transfer or the existence of strong antiferromagnetic interactions.

**Crystal structure of CT-B:** The arrangement of **NDI-Δ** in the solid-state is very sensitive to solvent identity and concentration, as is the co-crystallization of **NDI-Δ** and **TTF**. Crystallization of **NDI-Δ** and **TTF** by the slow diffusion of hexane into a solution of **NDI-Δ**•**TTF** in  $\text{CHCl}_3$  leads to the formation of a CT complex of **NDI-Δ**•**TTF** in a 2 : 3 mole ratio. **CT-B** crystallizes (Figure 9a) in a trigonal  $P32_1$  space group with two crystallographically distinct **NDI-Δ** molecules in the asymmetric unit. The two crystallographically distinct **NDI-Δ** molecules display a perpendicular rotation angle of  $60^\circ$  (a 3-fold screw axis) as a result of the stabilization by three pairs of self-complementary [C–H $\cdots$ O] interactions (mean  $d_{[\text{C-H}\cdots\text{O}]} = 3.25 \text{ \AA}$ ; mean  $\theta_{[\text{C-H}\cdots\text{O}]} = 162^\circ$ ) between the **NDI** units. The propagation of these hydrogen bonds along the *c*-axis leads to the formation of supramolecular nanotubes (Figure 9b) similar to those observed in other superstructures when a structure-directing 1,2-dihaloethane solvent is utilized.<sup>37</sup> In keeping with the superstructure of **NDI-Δ**• $\text{CHCl}_3$ , the cavity of **NDI-Δ** macrocycle in the **CT-B** superstructure contains (Figure 9a) molecules of  $\text{CHCl}_3$ . Apparently, **NDI-Δ** has stronger affinity to bind  $\text{CHCl}_3$  than **TTF**. Titration of **TTF** into a  $\text{CHCl}_3$  solution of **NDI-Δ** did not result (Figure S19) in any change of the aromatic chemical shift of the **NDI** protons in the  $^1\text{H}$  NMR spectrum, while titration of  $\text{CHCl}_3$  into a MeCN solution of **NDI-Δ** resulted in a strong shift of the aromatic protons, indicative (Figure S21) of the binding ( $K_a = 15 \text{ M}^{-1}$ ) of  $\text{CHCl}_3$  inside the **NDI-Δ** cavity. These data support the favorable interaction of chlorinated solvents through [Cl $\cdots$  $\pi$ (**NDI**)] and [Cl $\cdots$ H(**NDI**)] contacts. Surprisingly, one **NDI-Δ** of the two crystallographically distinct molecules interacts with three **TTF** molecules through face-to-face [ $\pi \cdots \pi$ ] interactions of  $3.27(1) \text{ \AA}$  and [C–H(cyclohexane) $\cdots$  $\pi$ (**TTF**)] interactions of  $2.88(1) \text{ \AA}$  to form (Layer 1 in Figure 9c,d) a 2D D/A layer-like superstructure. The

second **NDI-Δ** interacts with  $\text{CHCl}_3$  solvent through a set of  $[\text{Cl}\cdots\pi(\text{NDI})]$  interactions (Layer 2 in Figure 9e,f). It is remarkable that, in the absence of **TTF**, **NDI-Δ** forms neither supramolecular nanotubes nor a layer-like superstructure, but the presence of **TTF** modulates the packing to yield supramolecular nanotubes and layer-like superstructures. In the **D/A** layer (Layer 1), one structurally well-ordered  $\text{CHCl}_3$  molecule interacts with **TTF** through  $[\text{Cl}\cdots\text{S}]$  contacts of 3.55(2) Å (VDW radii = 3.55 Å) to form (Figure 9c, Figure S6a,b) a 2D network superstructure. The  $\text{CHCl}_3$  molecules are arranged (Figure 9c, Figure S8a) in a hexagonal fashion and can be considered as the vertices of a regular hexagon. In the ATs, these solvent-based regular hexagons are arranged in a *P6m* symmetry where three hexagons share same vertices. The second crystallographically distinct **NDI-Δ** interacts with  $\text{CHCl}_3$  solvent through a set of  $[\text{Cl}\cdots\pi(\text{NDI})]$  and  $[\text{Cl}\cdots\text{H-C(Cyclohexane)}]$  interactions. The **NDI-Δ** triangle also displays (Figure 9e,f) a vertex-to-edge tiling in the *ab*-plane. In Layer 2, by contrast, the two  $\text{CHCl}_3$  lattice molecules interact through  $[\text{Cl}\cdots\text{Cl}]$  bonds of 3.509(7) and 4.24(1) Å (VDW radii = 3.5 Å) to form (Figure 9e, Figure S7a) supramolecular  $\text{CHCl}_3$ -based triangles. These triangles tessellate in hexagonal fashion (*P6m* symmetry) through  $[\text{Cl}\cdots\text{Cl}]$  interactions to form (Figure S7) a hexagonal grid of solvent, similar to those found in the **D/A** layer (Layer 1). The two distinct layers—DADADA (Layer 1) and AAAA (Layer 2)—in the *ab*-plane can be represented schematically (Figure S8a,b) as a triangular grid of **NDI-Δ** inside a hexagonal grid of  $\text{CHCl}_3$ . Certainly, the interplay between the molecular structures of the **NDI-Δ** and the honeycomb supramolecular arrangement of the  $\text{CHCl}_3$  through a set of  $[\text{Cl}\cdots\text{Cl}]$  and  $[\text{Cl}\cdots\text{S(TTF)}]$  interactions plays a crucial role in the 2D packing of **CT-B**. Powder-XRD measurements show (Figure S13) the semi-crystalline nature of **CT-B** after removal of solvent, supporting the fragile nature of the crystal structure. Along the *c*-axis these layers alternate to form DADA-AAAA-DADA-AAAA stacking motifs (Figure S9). The **TTF**

molecule is relatively flat with a bending angle of the dithiol rings of  $\sim 5.6^\circ$  and a C=C bond length of 1.35(1) Å which is indicative of a partial charge transfer from **TTF** to **NDI-Δ**. EPR spectroscopy confirmed (Figure S26) the ionic state of the **CT-B** complex. The absence of a long-range propagation of the CT interactions between the NDI units and the **TTF** molecules, however, might hamper electron transport in this material.

**Crystal structure of CT-C:** The co-crystal **CT-C** was formed either by (i) slow diffusion of Et<sub>2</sub>O or hexane into a solution of **NDI-Δ** and **TTF** solubilized in CH<sub>2</sub>Cl<sub>2</sub> or (ii) slow evaporation of CH<sub>2</sub>Cl<sub>2</sub>. Once again, we found (Figure 10a) that the use of chlorinated solvents prevented **TTF** from entering the cavity of **NDI-Δ**. <sup>1</sup>H NMR Titration of **TTF** into a solution of **NDI-Δ** in CH<sub>2</sub>Cl<sub>2</sub> did not display a significant chemical shift of the protons, indicating (Figure S17) the lack of any binding of **TTF** inside **NDI-Δ**. **CT-C** crystallizes in the monoclinic *P2<sub>1</sub>/n* space group with three **TTF** molecules and one **NDI-Δ** molecule in the asymmetric unit (Figure 10a). Again, stacking of **NDI-Δ** displays perpendicular rotation angle of 60° around a 3-fold screw axis as a result of the stabilization by three pairs of self-complementary [C–H···O] interactions (mean d<sub>C···O</sub> = 3.25 Å and mean  $\theta_{[C-H\cdots O]} = 161^\circ$ ) between the NDI units (Figure S10a). The propagation of these hydrogen bounds along the *b*-axis leads (Figure S10b) to the formation of supramolecular nanotubes similar to those of **CT-B**. Unlike **CT-A**, however, in which only two edges of the **NDI-Δ** interact with **TTF** molecules, while the third edge interacts by [NDI···NDI] [π···π] interactions, in **CT-C**, each face of **NDI-Δ** interacts with one **TTF** molecule in a perpendicular face-to-face fashion (Figure 10a). The [π···π] distances between **TTF** and NDI units are in the range of 3.1(1)–3.28(4) Å (VDW radii = 3.4 Å). Propagation of these CT interactions in the *ac*-plane leads (Figure 10b) to the formation of 2D layer-like superstructure. The three **TTF** molecules interact through close S···S contacts of 3.48(8)–3.70(8) Å to form (Figure 10c) a supramolecular

triangle (TTF- $\Delta$ ). This TTF- $\Delta$  is a semi-regular triangle with length edges in the range of 6.4–6.7 Å, similar to those of the supramolecular triangles of CHCl<sub>3</sub> in **CT–B** (6.89 and 6.09 Å). According to the ATs, the two polygons **NDI- $\Delta$**  and TTF- $\Delta$  adopt (Figure 10c) a triangular tessellation pattern in the *ab*-plane with two different triangles. This 2D geometrical packing leads to the propagation of the CT interactions in a 2D layer. The TTF- $\Delta$  interact through unidirectional S···S contacts of 3.89(2) and 3.19(1) Å to form (Figure S10c) supramolecular chains. As a result of the rotational symmetry of two **NDI- $\Delta$**  along the *c*-axis, the TTF- $\Delta$  are arranged in hexagonal fashion with intermolecular [S···S] contacts propagating along one direction (Figure 10d, Figure S10c). Similar to the structure of **CT–B** in which solvent molecules form a supramolecular hexagonal shell, the TTF- $\Delta$  molecules form a hexagonal grid in which **NDI- $\Delta$**  stacks along the *b*-axis to form supramolecular nanotubes. A view of the superstructure along the *c*-axis illustrates (Figures S10e) the formation of stacked DADA layers. The absence of lattice solvent in **CT–C** increases the thermal stability of the material which is essential for single crystal electron-transport measurements. Indeed, thermal studies using VT powder XRD over a temperature range 100 to 400 K revealed (Figure S14) no change in the powder pattern, indicating the high stability of the material. Detailed structural analysis of the **TTF** molecules revealed that **TTF-1** is almost planar—the two pentagonal rings are slightly bent with an angle of 7.3°—with its C=C bond length elongated to 1.42(4) Å, corresponding to the radical cationic state. Both **TTF-2** and **TTF-3** are slightly curved with an angle between the two pentagonal rings of 13.5 and 15.4°, respectively. The C=C bond length of **TTF-2** of 1.35(3) Å is slightly more elongated than those of neutral **TTF**; this pattern is indicative of the partial CT while the C=C bond length of **TTF-3** is 1.32 (3) Å, similar to those of neutral **TTF** (1.33 Å). In this context, the close interaction between these **TTF** molecules through short [S···S] contacts below the VDW radii—VDW radius for [S···S] contact is 3.6 Å—is consistent

with the formation of a mixed-valence state between a radical cationic **TTF** (**TTF**<sup>+</sup>), a partially oxidized **TTF** and a neutral **TTF**. EPR Spectroscopic studies of **CT-C** in the solid-state and at room temperature revealed the existence of anisotropic signal similar to that for **CT-A**. Simulated results indicate (Figure S27) the existence of two types of paramagnetic centers, with a main component of  $g_{iso} = 2.0079$  and a minor component with  $g_{iso} = 2.004$ . Thus, the slight shift of the  $g_{iso}$ -value shows both the delocalization of the spin density as a result of the close intermolecular contacts and a contribution to the anisotropic shape of the EPR signal from chemically and crystallographically distinct paramagnetic components.

### ***Solution Spectroscopic Properties***

All solution samples of **NDI-Δ** and **TTF** for UV/Vis spectroscopic studies were measured at concentration of  $5 \times 10^{-5}$  M. In the first instance we have analyzed the UV-Vis spectra of **NDI-Δ** and **TTF** in MeCN separately. **NDI-Δ** exhibits (Figure 11) a vibronically structured absorption in the UV-Vis region with maxima at 340, 356 and 375 nm, indicative of the rigid structure of the **NDI-Δ**. These maxima correspond to  $\pi \rightarrow \pi^*$  transitions occurring in the NDI units. **TTF** exhibits typical absorption bands at 315, 372 and 454 nm associated with  $\pi \rightarrow \pi^*$  transitions.<sup>46</sup> In order to probe the effect of solvent in the formation of the **TTF**•**NDI-Δ** complex observed in the crystallographic studies, UV-Vis absorption studies of a mixture of **NDI-Δ** and **TTF** at a molar ratio of 1 : 3 and solubilized in different solvents (CHCl<sub>3</sub>, CH<sub>2</sub>Cl<sub>2</sub> and MeCN) have been recorded (Figure 11). The absorption spectra are dominated by **TTF** and **NDI-Δ**  $\pi \rightarrow \pi^*$  transitions which are influenced slightly by solvent polarity. As the solvent polarity decreases (MeCN > CH<sub>2</sub>Cl<sub>2</sub> > CHCl<sub>3</sub>), the absorption bands (356 and 375 nm) of **NDI-Δ** in MeCN undergo a small bathochromic shift. In CH<sub>2</sub>Cl<sub>2</sub>, the absorption bands of **NDI-Δ** are centered at 358 and 378 nm, while in CHCl<sub>3</sub> the bands are further shifted to 360 and 380 nm. This behavior indicates<sup>47</sup> that the bathochromic

shift is not associated with polarity but rather with the existence of intermolecular interactions with solvents ( $[\text{Cl}\cdots\pi]$  interactions). In the visible region of the spectra collected at room temperature in MeCN, a small CT band centered on 700 nm indicates the formation of the **TTF** $\subset$ **NDI- $\Delta$**  adduct. This band is absent in  $\text{CHCl}_3$  and  $\text{CH}_2\text{Cl}_2$  even at lower temperatures (Figures S23,S24). These data are consistent with the crystal structures and  $^1\text{H}$  NMR Titrations which have shown that  $\text{CHCl}_3$  and  $\text{CH}_2\text{Cl}_2$  have better affinity for the **NDI- $\Delta$**  cavity than does **TTF**. Previous studies<sup>47</sup> of catenanes containing **TTF** and **NDI** units have shown a CT band in the range of 400 to 500 nm, while **TTF** $\subset$ **CBPQT** (cyclobis(paraquat-*p*-phenylene)) has a stronger binding affinity and shows<sup>48</sup> a broad CT band centered at 830 nm. This behavior implies that the **NDI- $\Delta$**  cavity favors the interaction with **TTF** in MeCN and therefore enhances the CT character. Notably, a decrease in temperature leads to a significant red shift of the CT band to 1140 nm, corresponding to an increase of the binding between the **NDI- $\Delta$**  cavity and the **TTF** guest. Gas-phase DFT calculations revealed (Table S1) that the HOMO-LUMO charge separation ( $\Delta E_{\text{HOMO-LUMO}}$ ) between **NDI- $\Delta$**  and **TTF** is 1 eV (1240 nm). The magnitude of the charge separation between the two moieties is slightly affected by solvent polarity. In MeCN,  $\Delta E_{\text{HOMO-LUMO}} = 1.22$  eV (1016 nm) while in  $\text{CHCl}_3$  and  $\text{CH}_2\text{Cl}_2$   $\Delta E_{\text{HOMO-LUMO}} = 1.16$  eV (1068 nm). These theoretical studies are consistent with the experimentally determined CT band at 1140 nm for the **TTF** $\subset$ **NDI- $\Delta$**  complex.

### Solid-State Spectroscopic Studies

Solid-state absorption studies reproduce well the absorption band arising from the  $\pi\rightarrow\pi^*$  transitions of **NDI- $\Delta$** . New bands emerge in the visible, near (NIR) and far (FIR) IR regions. Crystallographic studies have revealed that the different **TTF** molecules in the crystal structure are either partially, fully oxidized or neutral. In addition, the existence of close intermolecular interactions between **TTF** molecules in the superstructures might affect the overall electronic

properties through the formation of mixed-valence forms between radical and neutral **TTF** species. Therefore, absorption spectra are expected to display broad bands on account of the contributions from different components. Although, all the crystal structures **CT-A**, **CT-B** and **CT-C** display the existence of face-to-face  $[\pi \cdots \pi]$  interactions between **NDI** units and **TTF**, the electronic properties of these materials are different. For **CT-A**, Figure 12 reveals a broad absorption band in a range 500 to 2700 nm ( $\lambda_{\max} = 835$  nm). Solid-state EPR Spectroscopy revealed that **CT-A** has significant CT character which implies the existence of **TTF**<sup>+</sup> and **NDI**<sup>−</sup> species. It has been reported<sup>49</sup> previously that **TTF**<sup>+</sup> has an absorption band at 480 nm while **NDI**<sup>−</sup> absorbs at 490, 700 and 790 nm. In addition, solution studies revealed the existence of a CT band at 1140 nm associated with the formation of a host-guest complex. Therefore, the origin of this band may be from a mixture of the different components (radical and neutral species) combined with the CT band of **TTF**–**NDI**–**Δ**. Time-dependent DFT (TDDFT) investigations also reproduce (Figure S33) the CT absorption band with a calculated broad band centered at 1200 nm associated with the transition from HOMO orbitals which are **TTF**-based to LUMO orbitals which are **NDI**–**Δ**-based (Figure S34, Table S2). Other investigations<sup>50</sup> reported the emergence of the CT band at 900 nm when an **NDI**-based MOF was doped with **TTF**, leading to the decrease of the optical band gap from 2.5eV (undoped) to 1eV (doped). Notably, the absorption spectrum of **CT-B** does not display these features. A shoulder can be observed at 750 nm, similar to the band at 700 nm observed in MeCN solution. The absence of close  $[\text{S} \cdots \text{S}]$  interactions between the **TTF** molecules and the absence of  $[\pi \cdots \pi]$  interactions between **NDI**–**Δ** units makes the assignment of the absorption band at 750 nm to a CT between **TTF** and **NDI**–**Δ**. Beyond doubt, crystallographic studies revealed that the C=C bond length is 1.35(1) Å—i.e., it is slightly more elongated than those of neutral **TTF** (1.33 Å)—confirming a partial CT. Clearly, the inclusion of the **TTF** inside the cavity of **NDI**–**Δ**

enhances the CT behavior leading to the formation of radical species which absorb in the NIR and FIR regions.

The crystal structure of **CT-C** revealed similar interactions of **TTF** molecules with **NDI-Δ**, while solid-state EPR spectroscopy revealed that the complex has an ionic state. Whereas in the **CT-A** structure, two **TTF** molecules interact with **NDI-Δ** externally and one **TTF** is localized inside the cavity, in **CT-C**, all three edges of **NDI-Δ** interact with **TTF** externally while the cavity is occupied by  $\text{CH}_2\text{Cl}_2$  solvent. **CT-C** displays (Figure 12) a dominant broad absorption band in the FIR region of the solid-state spectrum centered at 2500 nm. A small absorption band similar to that for **CT-A** is observed at 835 nm, consistent with the existence of **TTF**<sup>•+</sup> and **NDI-Δ**<sup>•-</sup> species and CT interactions. The crystal superstructure revealed that three **TTF** molecules interact through a set of [S···S] contacts to form a supramolecular **TTF** triangle (**TTF-Δ**). In addition, from the C=C bond lengths we can infer that one **TTF** molecule is in its radical cationic state while the two other **TTF** molecules are, respectively, partially oxidized and in a neutral state. In this context, the origin of the FIR absorption band can be attributed to the mixed-valence character of the **TTF-Δ**. In order to confirm the electronic configuration of **TTF-Δ**, we performed TDDFT studies using two electronic configurations—namely, (i) **TTF-Δ**<sup>2•+</sup>, where two **TTF** molecules are in a radical cationic state while the third **TTF** is neutral, and (ii) **TTF-Δ**<sup>•+</sup>, where one **TTF** is in a radical cationic state while the other two molecules are neutral. TDDFT calculations on **TTF-Δ**<sup>2•+</sup>, using a broken-symmetry singlet-state approach at the UB3LYP/6-31G\*+ basis set, revealed (Figure S35, Table S3) the existence of transitions at 3479 and 2802 nm with an oscillator factor of > 0.05. Both transitions involve orbitals from the three **TTF** components of **TTF-Δ**<sup>2•+</sup>. The SOMO-SUMO transition for each **TTF** is displayed (Figure S36, Tables S4,S5) at 563 and 547 nm, consistent with literature values.<sup>51</sup> Simulation of the absorption band using the electronic configuration **TTF-Δ**<sup>•+</sup>

has proved unsuccessful with respect to reproducing the band at 2500 nm (Figure S37, Table S6). Previous studies reported<sup>52</sup> the observation of a similar band at 2500 nm for  $(TTF)_3[TTF(CO_2H)_2(CO_2)_2]$ , which is composed of two  $TTF^{+}$  cations and one neutral  $TTF$  molecule along with one  $TTF(CO_2H)_2(CO_2^-)_2$  anion. The crystal superstructure was not reported, however, preventing detailed analysis of the structure-electronic properties relationship. Other studies<sup>53</sup> on mechanically interlocked TTF-based catenanes have noted the observation of a broad absorption band at 2100 nm, associated with the mixed-valence  $(TTF)_2^{2+}$  dimer. In this context, the triangular geometry of **NDI-Δ** combined with careful control of the crystallization conditions can lead to the formation CT complexes with different electronic properties. In particular, the generation of mixed-valence organic materials in the solid-state augurs well for their use in organic and optoelectronic devices.

## ■ CONCLUSIONS

We have investigated the effects of molecular tiling of an electronically-active **NDI-Δ** and **NDI-Δ•TTF** CT co-crystals through careful control of the crystallization conditions. The in-plane tiling of **NDI-Δ** is driven by the  $[\pi \cdots \pi]$  interactions between the **NDI-Δ**. While chlorinated solvents ( $CH_2Cl_2$ ,  $CHCl_3$ ) have a strong tendency to form  $[Cl \cdots \pi]$  interactions which compete with the  $[\pi \cdots \pi]$  interactions between the NDI units, leading to the disturbance of the in plane 2D tiling of the **NDI-Δ**, in non-halogenated solvents (MeCN), **NDI-Δ** is polymorphic and crystallizes into three different polymorphs (**α-NDI-Δ**, **β-NDI-Δ** and **γ-NDI-Δ**) depending on the solute concentrations. Crystallographic studies revealed that honeycomb triangular (**β-NDI-Δ**) and hexagonal tiling of the **NDI-Δ** is enthalpically favorable. Fast crystallization of the **NDI-Δ** leads to the formation of the **α** polymorph, while dilution of the solute solutions leads to the formation of a semi-regular or

regular ATs through 2D  $[\pi \cdots \pi]$  interactions between the NDI units. The  $\beta$  polymorph adopts a honeycomb triangular tiling with 3+3 symmetry in the AT, whilst the  $\gamma$  polymorph adopts a unique tiling where six **NDI- $\Delta$**  self-assemble to form a regular supramolecular hexagon (*hex-NDI- $\Delta$* ) which tessellate in a *P632* symmetry in the ATs.

Co-crystallisation of the electron-poor **NDI- $\Delta$**  with a strong electron donor, such as **TTF**, leads systematically to the formation of a 2D tiling pattern as the result of the strong directing CT interactions between the NDI and **TTF** moieties. The molecular arrangement of the **NDI- $\Delta$**  and **TTF** is also influenced by solvent accommodation. Utilization of non-halogenated solvents leads to the inclusion of **TTF** inside the cavity of the **NDI- $\Delta$** , while halogenated solvents prevent the **TTF** inclusion. The crystal packing in **CT-A** display a 2D propagation of CT interactions, and the ionic character of this complex has been confirmed through spectroscopic and SQUID magnetometry studies. We have demonstrated that a careful control of the crystal growth conditions, combined with the intrinsic triangular geometry of the **NDI- $\Delta$** , leads to the formation of mixed-valence **TTF- $\Delta^{2+}$**  superstructures which display a small optical band gap of 0.36 eV. The results provide useful insight into the control of packing geometries of regular and semi-regular molecular tiling using regular polygon building blocks. More broadly, the insights and lessons gained from the triangular NDI system suggest pathways for the deterministic design of a new class of 2D materials, thereby significantly expanding the structural phase space and thus potential properties and applications in organic electronics. The experimental realization of synthetic 2D polymorphs of **NDI- $\Delta$**  and fine-tuning the CT complexes, involved in the packing of **NDI- $\Delta$**  and **TTF**, anticipates a number of opportunities. Most apparently, the ability to modify the electronic properties through crystal engineering promises to unleash several fundamental and technological advances for the future design of supramolecular 2D organic materials.

## ■ ASSOCIATED CONTENT

### Supporting Information

Experimental details, including synthesis, NMR and supportive figures. This material is available free of charge through the Internet at <http://pubs.acs.org>.

## ■ AUTHOR INFORMATION

### Corresponding Author

\*stoddart@northwestern.edu

### Author Contributions

All authors have given approval to the final version of the manuscript.

### Notes

The authors declare no competing financial interest.

### ABBREVIATIONS

(Molecules are shown in bold whilst the other abbreviations are kept non-bolded). **TTF**, tetrathiafulvalene; **NDI-Δ**, naphthalenediimide triangle; **TCNQ**, tetracyanoquinodimethane; **CBPQT**, cyclobis(paraquat-p-phenylene); **TTF-Δ**, Tetrathiafulvalene triangle; **NDI**, naphthalenediimide; **QCs**, quasi-crystalline structures; **ATs**, archimedean tilings; **EPR**, electron paramagnetic resonance; **SOMO**, single occupied molecular orbital; **HOMO**, highest occupied molecular orbital; **LUMO**, lowest unoccupied molecular orbital; **SUMO**, single unoccupied molecular orbital; **SQUID**, superconducting quantum interference device; **VDW**, Van der Waals; **MOF**, metal-organic framework; **1D**, two-dimensional; **2D**, two-dimensional; **3D**, three-dimensional; **A**, acceptor; **D**, donor; **CT**, charge transfer.

## ■ ACKNOWLEDGEMENTS

We thank the personnel in the Integrated Molecular Structure Education and Research Center (IMSERC) at Northwestern University (NU) for their assistance in the collection of the data. The research conducted in the Stoddart laboratory is part of the Joint Center of Excellence in Integrated Nano-Systems (JCIN) at King Abdulaziz City of Science and Technology (KACST) and Northwestern University (NU). This project was also supported in the Wasielewski laboratory by the National Science Foundation under grant number DMR-1710104 (M.R.W.). The authors would like to thank both KACST and NU for their continued support of this research.

## ■ REFERENCES

- (1) (a) Grabar, A. *The Art of The World: Art of the Byzantine Empire*; Greystone Press: New York, **1967**. (b) Grünbaum, B.; Shephard, G. C. *Tilings and Patterns*; W. H. Freeman & Co.: New York, NY, USA, **1986**. (c) Chavey, D. Tilings by Regular Polygons 2. A Catalog of Tilings. *Comput Math Appl.* **1989**, *17*, 147–165.
- (2) (a) Kepler, J. *Harmonices mundi; Johannes Planck*; Linzs, **1619**.
- (3) Millan, J. A.; Ortiz, D.; van Anders, G.; Glotzer, S. C. Self-Assembly of Archimedean Tilings with Enthalpically and Entropically Patchy Polygons. *ACS Nano.* **2014**, *8*, 2918–2928.
- (4) Shechtman, D.; Blech, I.; Gratias, D.; Cahn, J. W. Metallic Phase with Long-Range Orientational Order and No Translational Symmetry. *Phys. Rev. Lett.* **1984**, *53*, 1951–1953. (b) Levine, D.; Steinhardt, P. J. Quasicrystals: A New Class of Ordered Structures. *Phys. Rev. Lett.* **1984**, *53*, 2477–2480.
- (5) Ueda, K.; Dotera, T.; Gemma, T. Photonic Band Structure Calculations of Two-Dimensional Archimedean Tiling Patterns. *Phys. Rev. B.* **2007**, *75*, 195122.
- (6) Ramirez, A. P. Strongly Geometrically Frustrated Magnets. *Annu. Rev. Mater. Sci.* **1984**, *24*, 453–480.
- (7) Tsai, A. P.; Yoshimura, M. Highly Active Quasi-Crystalline Al-Cu-Fe Catalyst for Steam Reforming of Methanol. *Appl. Catal. A.* **2001**, *214*, 237–241.
- (8) (a) Zhang, F.; Liu, Y.; Yan, H. Complex Archimedean Tiling Self-Assembled from DNA Nanostructures. *J. Am. Chem. Soc.* **2013**, *135*, 7458–7461. (b) Zhang, F.; Jiang, S.; Li, W.; Hunt, A.; Liu, Y.; Yan, H. Self-Assembly of Complex DNA Tessellations by Using Low-Symmetry Multi-Arm DNA Tiles. *Angew. Chem. Int. Ed.* **2016**, *128*, 9006–9009. (c) Matthies, M.; Agarwal, N. P.; Poppleton, E.; Joshi, F. M.; Šulc, P.; Schmidt, T. L. Triangulated Wireframe Structures Assembled Using Single-Stranded DNA Tiles. *ACS Nano.* **2019**, *13*, 1839–1848.

- (9) Tschierske, C. Liquid Crystal Engineering—New Complex Mesophase Structures and Their Relations to Polymer Morphologies, Nanoscale Patterning and Crystal Engineering. *Chem. Soc. Rev.* **2007**, *36*, 1930–1970.
- (10) Talapin, D. V.; Shevchenko, E. V.; Bodnarchuk, M. I.; Ye, X.; Chen, J.; Murray, C. B. Quasicrystalline Order in Self-Assembled Binary Nanoparticle Superlattices. *Nature* **2009**, *461*, 964–967.
- (11) (a) Asari, T.; Arai, S.; Takano, A.; Matsushita, Y. Archimedean Tiling Structures from ABA/CD Block Copolymer Blends Having Intermolecular Association with Hydrogen Bonding. *Macromolecules* **2006**, *39*, 2232–2237.
- (12) Shen, Y.; Deng, K.; Yang, S.; Qin, B.; Cheng, S.; Zhu, N.; Ding, J.; Zhao, D.; Liu, J.; Zeng, Q.; Wang, C. Triangular-Shaped Molecular Random Tiling and Molecular Rotation in Two-Dimensional Glassy Networks. *Nanoscale* **2014**, *6*, 7221–7225.
- (13) Destoop, I.; Ghijssens, E.; Katayama, K.; Tahara, K.; Mali, K. S.; Tobe, Y.; De Feyter, S. Solvent-Induced Homochirality in Surface-Confined Low-Density Nanoporous Molecular Networks. *J. Am. Chem. Soc.* **2012**, *134*, 19568–19571.
- (14) Iritani, K.; Ikeda, M.; Yang, A.; Tahara, K.; Hirose, K.; Moore, J. S.; Tobe, Y. Hexagonal Molecular Tiling by Hexagonal Macrocycles at the Liquid/Solid Interface: Structural Effects on Packing Geometry. *Langmuir* **2017**, *33*, 12453–12462.
- (15) Xu, S.-Q.; Zhan, T.-G.; Wen, Q.; Pang, Z.-F.; Zhao, X. Diversity of Covalent Organic Frameworks (COFs): A 2D COF Containing Two Kinds of Triangular Micropores of Different Sizes. *ACS Macro Lett.* **2016**, *5*, 99–102.
- (16) Ng, C.-F.; Chow, H.-F.; Mak, T. C. W. Organic Molecular Tessellations and Intertwined Double Helices Assembled by Halogen Bonding. *CrystEngComm.* **2019**, *21*, 1130–1136.
- (17) Ferraris, J. P.; Poehler, T. O.; Bloch, A. N.; Cowan, D. O. Synthesis of the Highly Conducting Organic Salt: Tetramethyltetrathiofulvalenium – Tetracyano–Quinodimethanide. *Tetrahedron*

*Lett.* **1973**, *14*, 2553–2556.

- (18) Yamada, J.-i.; Akutsu, H. New Trends in the Synthesis of  $\pi$ -Electron Donors for Molecular Conductors and Superconductors. *Chem. Rev.* **2004**, *104*, 5057–5084
- (19) (a) Girlando, A.; Painelli, A.; Bewick, S. A.; Soos, Z. G. Charge Fluctuations and Electron-Phonon Coupling in Organic Charge-Transfer Salts with Neutral-Ionic and Peierls Transitions. *Synth. Met.* **2004**, *141*, 129–138. (b) Horiuchi, S.; Tokura, Y. Organic Ferroelectrics. *Nat. Mater.* **2008**, *7*, 357–366.
- (20) (a) Kagawa, F.; Horiuchi, S.; Matsui, H.; Kumai, R.; Onose, Y.; Hasegawa, T.; Tokura, Y. Electric-Field Control of Solitons in a Ferroelectric Organic Charge-Transfer Salt. *Phys. Rev. Lett.* **2010**, *104*, 227602. (b) Kobayashi, K.; Horiuchi, S.; Kumai, R.; Kagawa, F.; Murakami, Y.; Tokura, Y. Electronic Ferroelectricity in a Molecular Crystal with Large Polarization Directing Antiparallel to Ionic Displacement. *Phys. Rev. Lett.* **2012**, *108*, 237601. (c) Horiuchi, S.; Kobayashi, K.; Kumai, R.; Ishibashi, S. Ionic Versus Electronic Ferroelectricity on Donor-Acceptor Molecular Sequence. *Chem. Lett.* **2014**, *43*, 26–35.
- (21) Tayi, A. S.; Shveyd, A. K.; Sue, A. C.-H.; Szarko, J. M.; Rolczynski, B. S.; Cao, D.; Kennedy, T. J.; Sarjeant, A. A.; Stern, C. L.; Paxton, W. F.; Wu, W.; Dey, S. K.; Fahrenbach, A. C.; Guest, J. R.; Mohseni, H.; Chen, L. X.; Wang, K. L.; Stoddart, J. F.; Stupp, S. I. Room-Temperature Ferroelectricity in Supramolecular Networks of Charge-Transfer Complexes. *Nature* **2012**, *488*, 485–489.
- (22) Novoselov, K. S. Electric Field Effect in Atomically Thin Carbon Films. *Science* **2004**, *306*, 666–669.
- (23) Xiufeng, S.; Jinlian, H.; Haibo, Z. Two-Dimensional Semiconductors: Recent Progress and Future Perspectives. *J. Mater. Chem. C* **2013**, *1*, 2952–2969.
- (24) Eftekhari, A. Tungsten Dichalcogenides (WS<sub>2</sub>, WSe<sub>2</sub>, and WTe<sub>2</sub>): Materials Chemistry and

Applications. *J. Mater. Chem. A* **2017**, *5*, 18299–18325.

- (25) (a) Xia, F.; Wang, H.; Xiao, D.; Dubey, M.; Ramasubramaniam, A. Two-Dimensional Material Nanophotonics, *Nat. Photonics* **2014**, *8*, 899–907. (b) Yu, L.; Lee, Y-H.; Ling, X.; Santos, J. G. S.; Shin, Y. C.; Lin, Y.; Dubey, M.; Kaxiras, E.; Kong, J.; Wang, H.; Palacios, T. Graphene/MoS<sub>2</sub> Hybrid Technology for Large-Scale Two-Dimensional Electronics. *Nano Lett.* **2014**, *14*, 3055–3063.
- (26) (a) Hana, Y.; Ge, Y.; Chao, Y.; Wang, C.; Wallace, G. G. Recent Progress in 2D Materials for Flexible Supercapacitors. *J. Energy Chem.* **2018**, *27*, 57–72. (b) Akinwande, D.; Petrone, N.; Hone, J. Two-Dimensional Flexible Nanoelectronics. *Nat. Commun.* **2014**, *5*, 5678.
- (27) (a) Würthner, F.; Stolte, M. Naphthalene and Perylene Diimides for Organic Transistors. *Chem. Commun.* **2011**, *47*, 5109–5115. (b) Zhan, X.; Facchetti, A.; Barlow, S.; Marks, T. J.; Ratner, M. A.; Wasielewski, M. R.; Marder, S. R. Rylene and Related Diimides for Organic Electronics. *Adv. Mater.* **2011**, *23*, 268–284. (c) Jones, B. A.; Facchetti, A.; Wasielewski, M. R.; Marks, T. J. Tuning Orbital Energetics in Arylene Diimide Semiconductors. Materials Design for Ambient Stability of n-Type Charge Transport. *J. Am. Chem. Soc.* **2007**, *129*, 15259–15278.
- (28) Hong, J.; Ha, Y. H.; Cha, H.; Kim, R.; Kim, Y. J.; Park, C. E.; Durrant, J. R.; Kwon, S.-K.; An, T. K.; Kim, Y-H. All-Small-Molecule Solar Cells Incorporating NDI-Based Acceptors: Synthesis and Full Characterization. *ACS Appl. Mater. Interfaces* **2017**, *9*, 44667–44677.
- (29) (a) Mukhopadhyay, P.; Iwashita, Y.; Shirakawa, M.; Kawano, S; Fujita, N.; Shinkai, S. Spontaneous Colorimetric Sensing of the Positional Isomers of Dihydroxynaphthalene in a 1D Organogel Matrix. *Angew. Chem. Int. Ed.* **2006**, *45*, 1592–1595. (b) Gu, P.-Y.; Wang, Z.; Liu, G.; Nie, L.; Ganguly, R.; Li, Y.; Zhang, Q. Synthesis, Physical Properties, and Sensing Behaviour of a Novel Naphthalenediimide Derivative Dyes. *Pigm.* **2016**, *131*, 224– 230.
- (30) (a) Al Kobaisi, M.; Bhosale, S. V.; Latham, K.; Raynor, A. M.; Bhosale, S. V. Functional Naphthalene Diimides: Synthesis, Properties, and Applications. *Chem. Rev.* **2016**, *116*, 11685–

- 11796, (b) Wu, Z. H.; Huang, Z. T.; Guo, R. X.; Sun, C. L.; Chen, L. C.; Sun, B.; Shi, Z. F.; Shao, X.; Li, H.; Zhang, H. L. 4,5,9,10-Pyrene Diimides: A Family of Aromatic Diimides Exhibiting High Electron Mobility and Two-Photon Excited Emission. *Angew. Chem., Int. Ed.* **2017**, *56*, 13031–13035.
- (31) Chen, D.; Avestro, A.-J.; Chen, Z.; Sun, J.; Wang, S.; Xiao, M.; Erno, Z.; Algaradah, M. M.; Nassar, M. S.; Amine, K.; Meng, Y.; Stoddart, J. F. A Rigid Naphthalenediimide Triangle for Organic Rechargeable Lithium-Ion Batteries. *Adv. Mater.* **2015**, *27*, 2907–2912.
- (32) Schneebeli, S. T.; Frasconi, M.; Liu, Z.; Wu, Y.; Gardner, D. M.; Strutt, N. L.; Cheng, C.; Carmieli, R.; Wasielewski, M. R.; Stoddart, J. F. Electron Sharing and Anion– $\pi$  Recognition in Molecular Triangular Prisms. *Angew. Chem. Int. Ed.* **2013**, *52*, 13100–13104.
- (33) Mizuno, A.; Shuku, Y.; Suizu, R.; Matsushita, M.; Tsuchiizu, M.; Mañeru, D. R.; Illas, F.; Robert, V.; Awaga, K. Discovery of the K4 Structure Formed by a Triangular  $\pi$  Radical Anion. *J. Am. Chem. Soc.* **2015**, *137*, 7612–7615.
- (34) Wu, Y.; Krzyaniak, M. D.; Stoddart, J. F.; Wasielewski, M. R. Spin Frustration in the Triradical Trianion of a Naphthalenediimide Molecular Triangle. *J. Am. Chem. Soc.* **2017**, *139*, 2948–2951.
- (35) Egli, M.; Gessner, R. V. Stereoelectronic Effects of Deoxyribose O4' on DNA Conformation. *Proc. Natl. Acad. Sci. U. S. A.* **1995**, *92*, 180–184.
- (36) Fang, X.; Yuan, X.; Song, Y.-B.; Wang, J.-D.; Lin, M.-J. Cooperative Lone Pair– $\pi$  and Coordination Interactions in Naphthalene Diimide Coordination Networks. *CrystEngComm.* **2014**, *16*, 9090–9095.
- (37) Liu, Z.; Liu, G.; Wu, Y.; Cao, D.; Sun, J.; Schneebeli, S. T.; Nassar, M. S.; Mirkin, C. A.; Stoddart, J. F. Assembly of Supramolecular Nanotubes from Molecular Triangles and 1,2-Dihalohydrocarbons. *J. Am. Chem. Soc.* **2014**, *136*, 47, 16651–16660.
- (38) (a) Kitaigorodskii, I. *Organic Chemical Crystallography*; Consultants Bureau: New York, **1961**. (b) Bernstein, J. *Polymorphism in Molecular Crystals*; Oxford University Press: Oxford,

UK, 2007.

- (39) Lu, C.; Li, Y.; Wang, L.-M.; Yan, H.-J.; Chen, L.; Wang, D. Rational Design of Two-Dimensional Covalent Tilings Using a C<sub>6</sub>-Symmetric Building Block via On-Surface Schiff Base Reaction. *Chem. Commun.* **2019**, *55*, 1326–1329.
- (40) Ostroverkhova, O. Organic Optoelectronic Materials: Mechanisms and Applications. *Chem. Rev.* **2016**, *116*, 13279–13412
- (41) (a) Guinonneau, P.; Kepert, C. J.; Bravic, G.; Chasseau, D.; Truter, M. R.; Kurmoo, M.; Day, P. Determining the Charge Distribution in BEDT-TTF Salts. *Synth. Met.* **1997**, *86*, 1973. (b) Umland, T. C.; Allie, S.; Kuhlman, T.; Coppens, P. Relation Between Geometry and Charge Transfer in Low-Dimensional Organic Salts. *J. Phys. Chem.* **1988**, *92*, 6456.
- (42) Wartelle, C.; Viruela, R.; Viruela, P. M.; Sauvage, F. X.; Salle, M.; Orti, E.; Levillain, E.; Le Derf, F. First Signals of Electrochemically Oxidized Species of TTF and TTM-TTF: A Study by in situ Spectroelectrochemical FTIR and DFT Calculations. *Phys. Chem. Chem. Phys.* **2003**, *5*, 4672–4679.
- (43) Matsuzaki, S.; Kuwata, R.; Toyoda, K. Raman Spectra of Conducting TCNQ Salts; Estimation of the Degree of Charge Transfer from Vibrational Frequencies. *Solid State Commun.* **1980**, *33*, 403–405.
- (44) (a) Yamamoto, S.; Pirillo, J.; Hijikata, Y.; Zhang, Z.; Awaga, K. Nanopore-Induced Host–Guest Charge Transfer Phenomena in a Metal–Organic Framework. *Chem. Sci.* **2018**, *9*, 3282–3289.
- (45) Cai, S.-L.; Zhang, Y.-B.; Pun, A. B.; He, B.; Yang, J.; Toma, F. M.; Sharp, I. D.; Yaghi, O. M.; Fan, J.; Zheng, S.-R.; Zhang, W.-G.; Liu, Y. Tunable Electrical Conductivity in Oriented Thin Films of Tetrathiafulvalene-Based Covalent Organic Framework. *Chem. Sci.* **2014**, *5*, 4693–4700.
- (46) Zhang, J.; Sun, B.; Wang, Q.; Zou, L. Novel Multi-Stimuli Responsive Molecules Based on Photochromic Bithienylethenes Containing the Tetrathiafulvalene Unit. *RSC Adv.* **2016**, *6*, 16598–16601.
- (47) Montoro, T.; Tardajos, G.; Guerrero, A.; Torres, D.-M.; Salgado, C.; Fernández, I.; Barcina,

J. O.  $\sigma$ -Hole $\cdots\pi$  and Lone Pair $\cdots\pi$  Interactions in Benzylic Halides. *Org. Biomol. Chem.* **2015**, *13*, 6194–6202.

(48) Cao, D.; Amelia, M.; Klivansky, L. M.; Koshkakaryan, G.; Khan, S. I.; Semeraro, M.; Silvi, S.; Venturi, M.; Credi, A.; Liu, Y. Probing Donor–Acceptor Interactions and Co-Conformational Changes in Redox Active Desymmetrized [2]Catenanes. *J. Am. Chem. Soc.* **2010**, *132*, 1110–1122.

(49) Zhao, Y.-L.; Trabolsia, A.; Stoddart, J. F. A Bistable Pretzelane. *Chem. Commun.* **2009**, 4844–4846.

(50) La Porte. N. T.; Martinez, J. F.; Chaudhuri, S.; Hedström, S.; Batista, V.S.; Wasielewski. M. R. Photoexcited Radical Anion Super-Reductants for Solar Fuels Catalysis. *Coord. Chem. Rev.* **2018**, *361*, 98–119.

(51) Guo, Z.; Panda, D. K.; Gordillo, Monica A.; Khatun, A.; Wu, H.; Zhou, W.; Saha, S. Lowering Band Gap of an Electroactive Metal–Organic Framework via Complementary Guest Intercalation. *ACS Appl. Mater. Interfaces* **2017**, *9*, 32413–32417.

(52) Mercier, N.; Giffard, M.; Pilet, G.; Allain, M.; Hudhomme, P.; Mabon, G.; Levillain, E.; Gorgues, A.; Riou, A. (TTF)<sub>2</sub>[TTF(CO<sub>2</sub>H)<sub>2</sub>(CO<sub>2</sub>)<sub>2</sub>]: A Wholly TTF Material Containing TTF Radical Cations and TTF Derived Anions. *Chem. Commun.* **2001**, 2722–2723.

(53) Spruell, J. M.; Coskun, A.; Friedman, D. C.; Forgan, R. S.; Sarjeant, A. A.; Trabolsi, A.; Fahrenbach, A. C.; Barin, G.; Paxton, W. F.; Dey, S. K.; Olson, M. A.; Benítez, D.; Tkatchouk, E.; Colvin, M. T.; Carmielli, R.; Caldwell, S. T.; Rosair, G. M.; Hewage, S. G.; Duclairoir, F.; Seymour, J. L.; Slawin, A. M. Z.; Goddard III, W. A.; Wasielewski, M. R.; Cooke, G.; Stoddart, J. F. Highly Stable Tetrathiafulvalene Radical Dimers in [3]Catenanes. *Nat. Chem.* **2010**, *2*, 870–879.

## Captions to Schemes and Figures

**Figure 1.** Schematic representation of (a) segregated  $\pi$ -stack CT structure. (b) Alternately stacked D/A molecules in a mixed-stacked CT assembly.

**Figure 2.** (a) Naphthalene carbodiimide triangle (**NDI- $\Delta$** ) with  $C_3$  molecular symmetry. (b) Expected tiling of the **NDI- $\Delta$**  through  $[\pi \cdots \pi]$  interactions and tiling of the **NDI- $\Delta$ :TTF** co-crystal through CT interactions.

**Figure 3.** Summary of the crystallization conditions utilized to isolate the different crystals of **NDI- $\Delta$** .

**Figure 4.** Summary of the crystallization conditions utilized to isolate the different **NDI- $\Delta$ :TTF** cocrystals.

**Figure 5.** Crystal superstructure of  **$\alpha$ -NDI- $\Delta$**  showing (a) two molecules (dimer) in the asymmetric unit interacting through  $[\pi \cdots \pi]$  interactions. (b) Hydrogen bonding  $[\text{C}=\text{O} \cdots \text{H}]$  between the **NDI- $\Delta$**  propagating along the *a*-axis (blue) *b*-axis (gold) to form zig-zag chains. Colors show symmetry equivalence.

**Figure 6.** Crystal superstructure of  **$\beta$ -NDI- $\Delta$**  with colors showing the symmetry equivalence between the different moieties. Hydrogen atoms are removed for the sake of clarity. (a) Two molecules (dimer) in the asymmetric unit interacting through  $[\pi \cdots \pi]$  interactions. (b) Hydrogen bonding  $[\text{C}=\text{O} \cdots \text{H}]$  between the **NDI- $\Delta$**  propagating along the *a*-axis to form tubular

superstructures. (c) Top view of six triangles around a vertex, 121212, leading a hexagonal superstructure. (d) Triangular tiling of the two symmetrically non-related **NDI-Δ** in the *bc*-plane. (e) Schematic representation of a semi-regular Archimedean triangular tiling with alternate colors.

**Figure 7.** Crystal superstructure of  $\gamma$ -**NDI-Δ** showing (a) Six triangles around a vertex, 111111, interacting through  $[\pi \cdots \pi]$  interactions to offer regular hexagonal superstructure **hex-NDI-Δ** (with one molecule of Et<sub>2</sub>O inside the **NDI-Δ** cavity). (b) Schematic representation of **hex-NDI-Δ**. (c) Hexagonal tiling of the hexagonal superstructure **hex-NDI-Δ** in the *ab*-plane with the *P6m* symmetry in the Archimedean hexagonal tilings. MeCN solvent forms a hexagonal shell surrounding the **hex-NDI-Δ**.

**Figure 8.** Crystal superstructure of **CT-A** showing (a) the asymmetric unit containing one **NDI-Δ** and 2.5 **TTF** molecules. The **TTF** inside the cavity was refined with an occupancy factor of 0.5. (b) Side view of the disordered **TTF** inside the  $(\text{NDI-}\Delta)_2$ . (c) Packing of the **NDI-Δ** and **TTF** in plane leading to a layer-like superstructure in the *cb*-plane. Colors show symmetry equivalence. Hydrogen atoms are removed for the sake of clarity.

**Figure 9.** Crystal superstructure of **CT-B** showing (a) The two crystallographically distinct **NDI-Δ** macrocycles interacting with three **TTF** molecules. Hydrogen atoms are removed for the sake of clarity. Colors illustrate the symmetry equivalence. (b) Hydrogen bonding [C=O $\cdots$ H] between the **NDI-Δ** propagating along the *c*-axis to form a tubular superstructure. (c) The arrangement of **NDI-Δ**, **TTF** and CHCl<sub>3</sub> molecule in the *ab*-plane with **TTF** and CHCl<sub>3</sub> interconnected through a 2D network of close [Cl $\cdots$ S] contacts. (d) Schematic representation of the vertex-to-edge packing

of the **NDI-Δ:TTF** to form a 2D superstructure (Layer 1). (e) Two symmetrically distinct  $\text{CHCl}_3$  molecules (purple and magenta) are connected through a set of  $[\text{Cl}\cdots\text{Cl}]$  contacts forming a supramolecular  $\text{CHCl}_3$  triangles ( $\text{CHCl}_3\text{-}\Delta$ ). These supramolecular  $\text{CHCl}_3\text{-}\Delta$  are arranged in hexagonal fashion to form a 2D hexagonal grid in which the **NDI-Δ** is tessellated. (f) Schematic representation of the vertex-to-edge packing of the **NDI-Δ** to form a 2D superstructure (Layer 2).

**Figure 10.** Crystal superstructure of **CT-C** showing (a) the asymmetric unit containing one **NDI-Δ** and three **TTF** molecules, with  $\text{CH}_2\text{Cl}_2$  in the cavity of **NDI-Δ**. Hydrogen atoms are removed for the sake of clarity and colors represent the symmetry equivalence. (b) Close  $\text{S}\cdots\text{S}$  interactions between the crystallographically distinct **TTF** molecules generating supramolecular isoscele triangles (**TTF-Δ**). (c) Packing of the **NDI-Δ** and **TTF-Δ** in the *ab*-plane to offer a *layer-like* superstructure with CT interactions propagating in the 2D plane. (d) Hexagonal arrangement of **TTF-Δ** as the result of the perpendicular rotation ( $C_3$ -fold symmetry) of two **NDI-Δ** along the *b*-axis. (e) Schematic representation of the irregular Archimedean triangular tiling of two different triangles (**NDI-Δ** and **TTF-Δ**) in a 2D network of CT interactions. (f) Schematic representation of the arrangement of two layers of **NDI-Δ** and **TTF-Δ** showing the Asterix shape of the  $(\text{NDI-}\Delta)_2$  surrounded by hexagonal packing the **TTF-Δ**.

**Figure 11.** (a) Absorption spectra of a 1:1 mole ratio of **NDI-Δ:TTF** mixture in different solvents. Absorption spectra of pure **TTF** and **NDI-Δ** in MeCN are recorded as references. (b) Absorption spectra of **NDI-Δ•TTF** measured at 20°C and -5°C.

**Figure 12.** (a) Room temperature solid-state absorption spectra of **NDI-Δ** (blue), **CT-A** (black), **CT-B** (red) and **CT-C** (green).

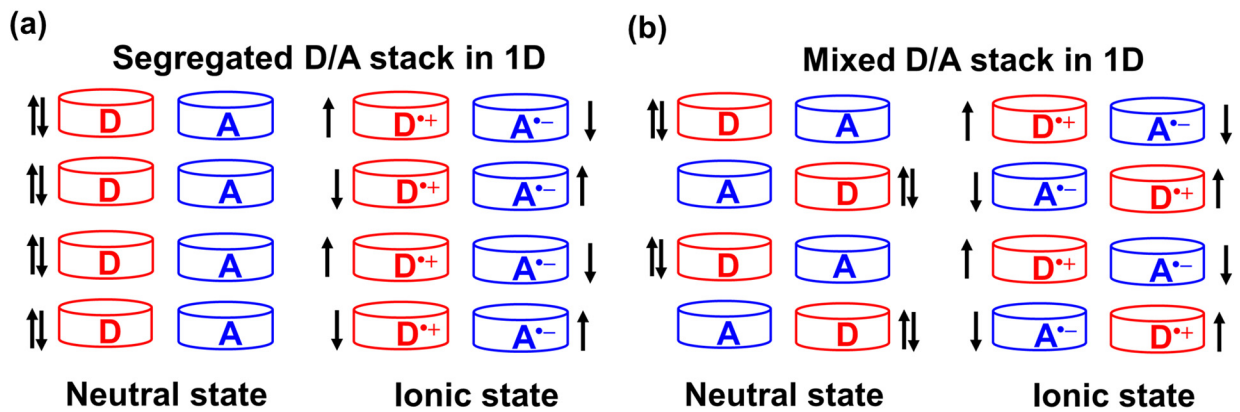


**Figure 1**

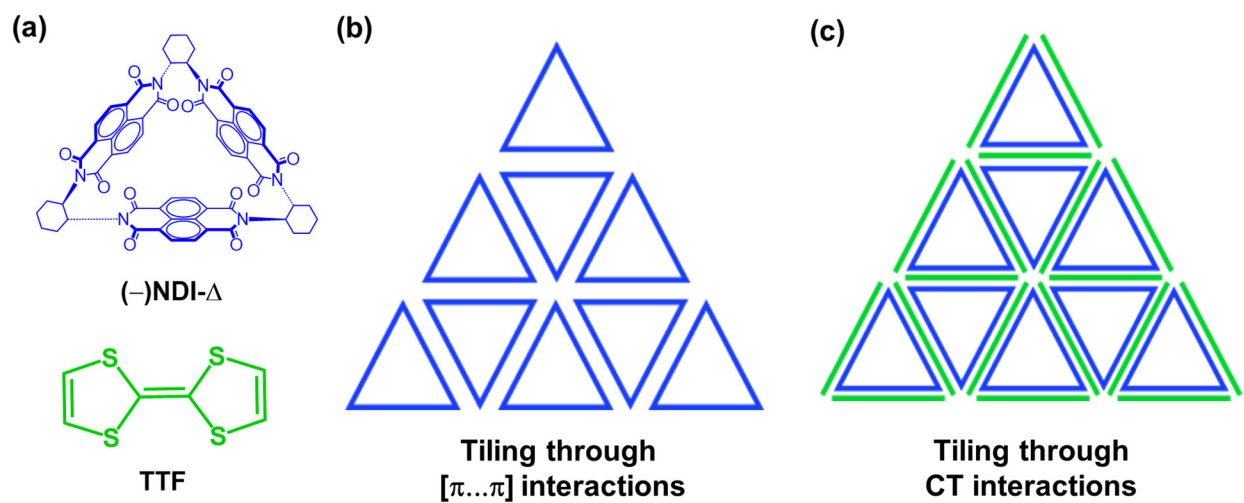


**Figure 2**

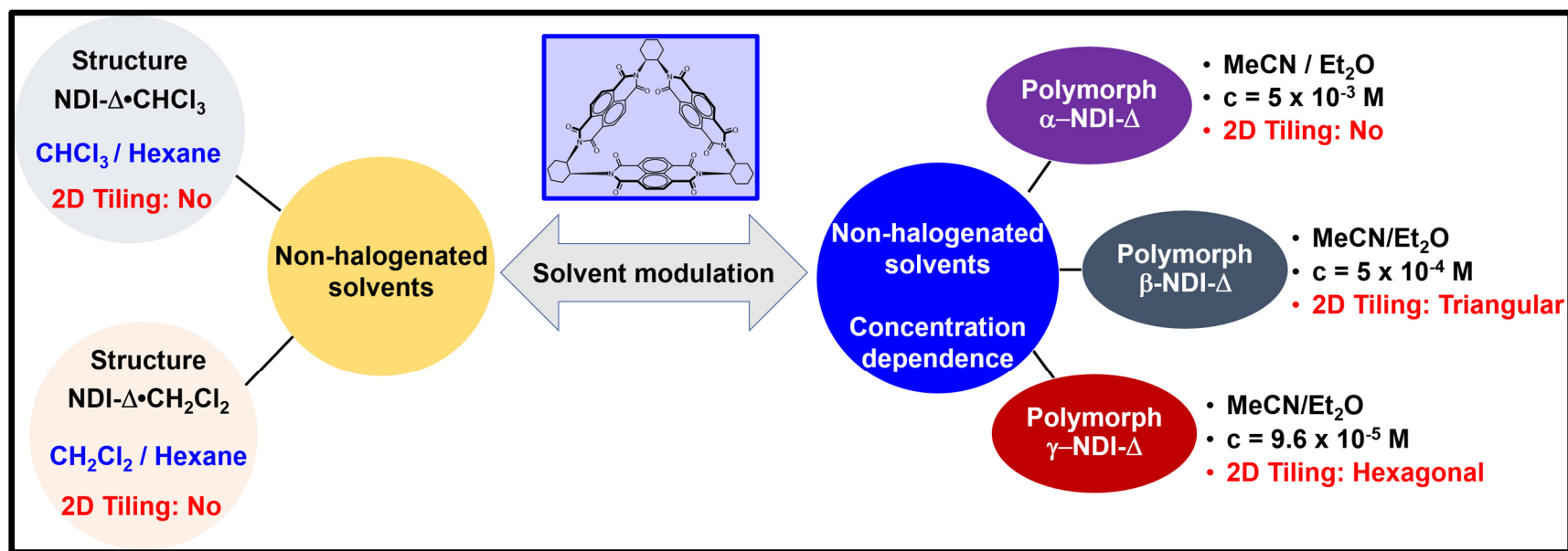


**Figure 3**

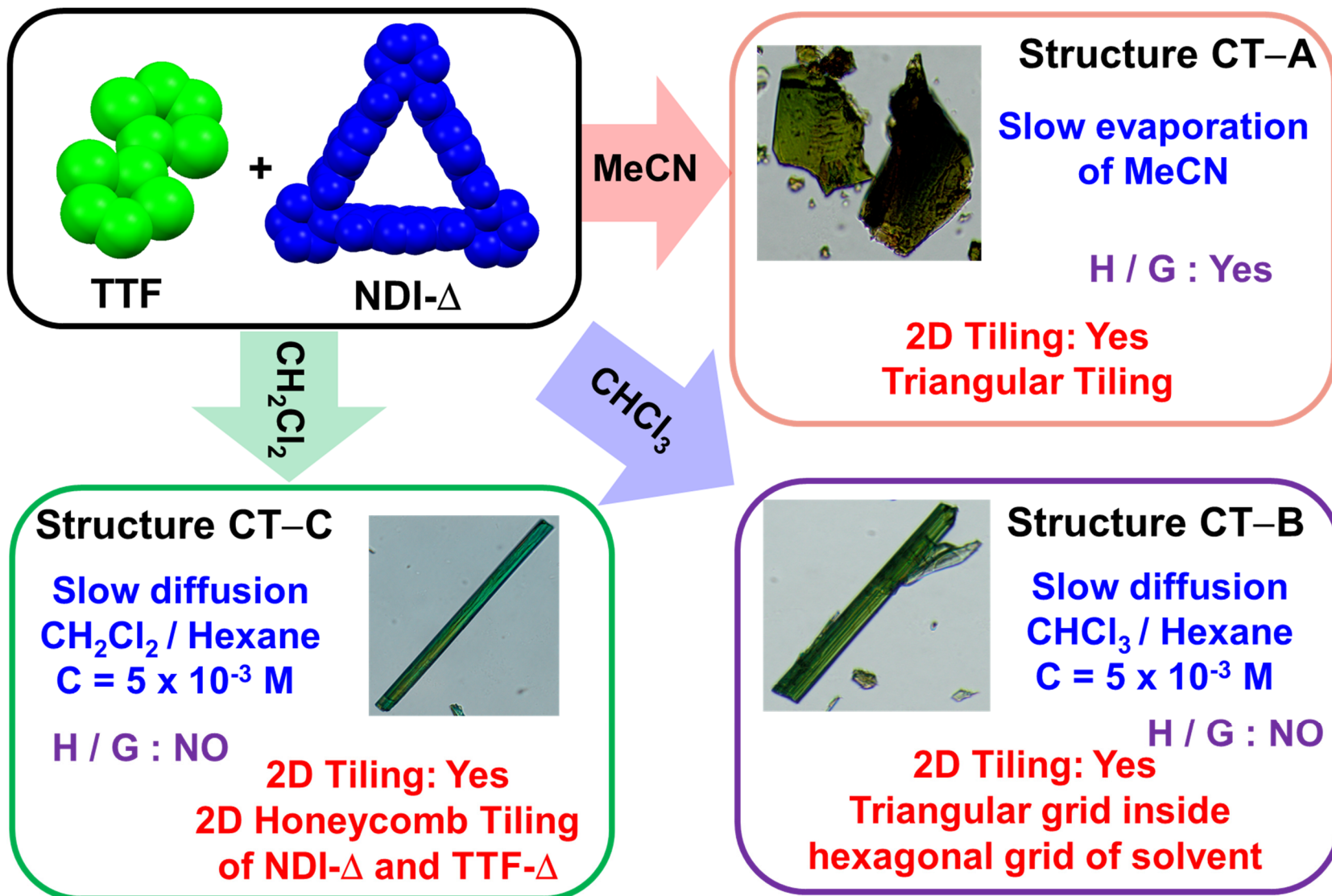
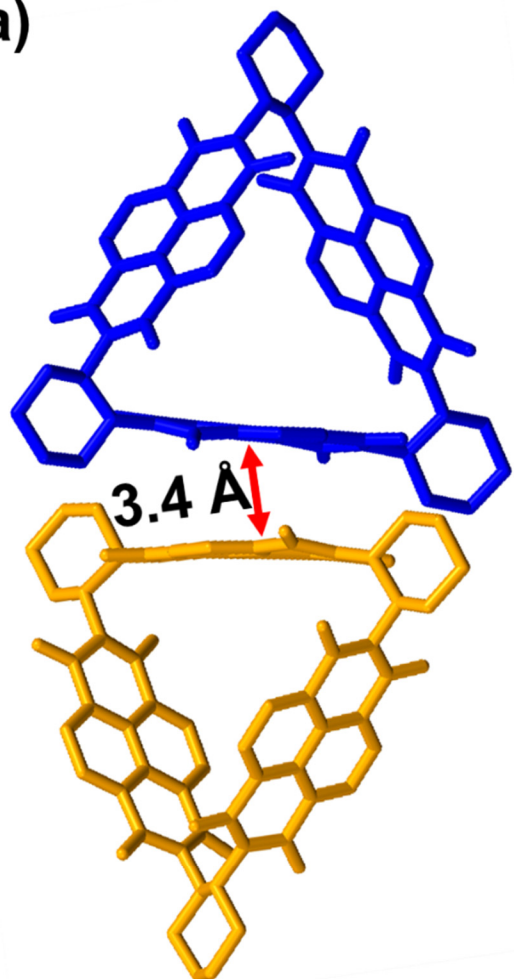


Figure 4

(a)



(b)

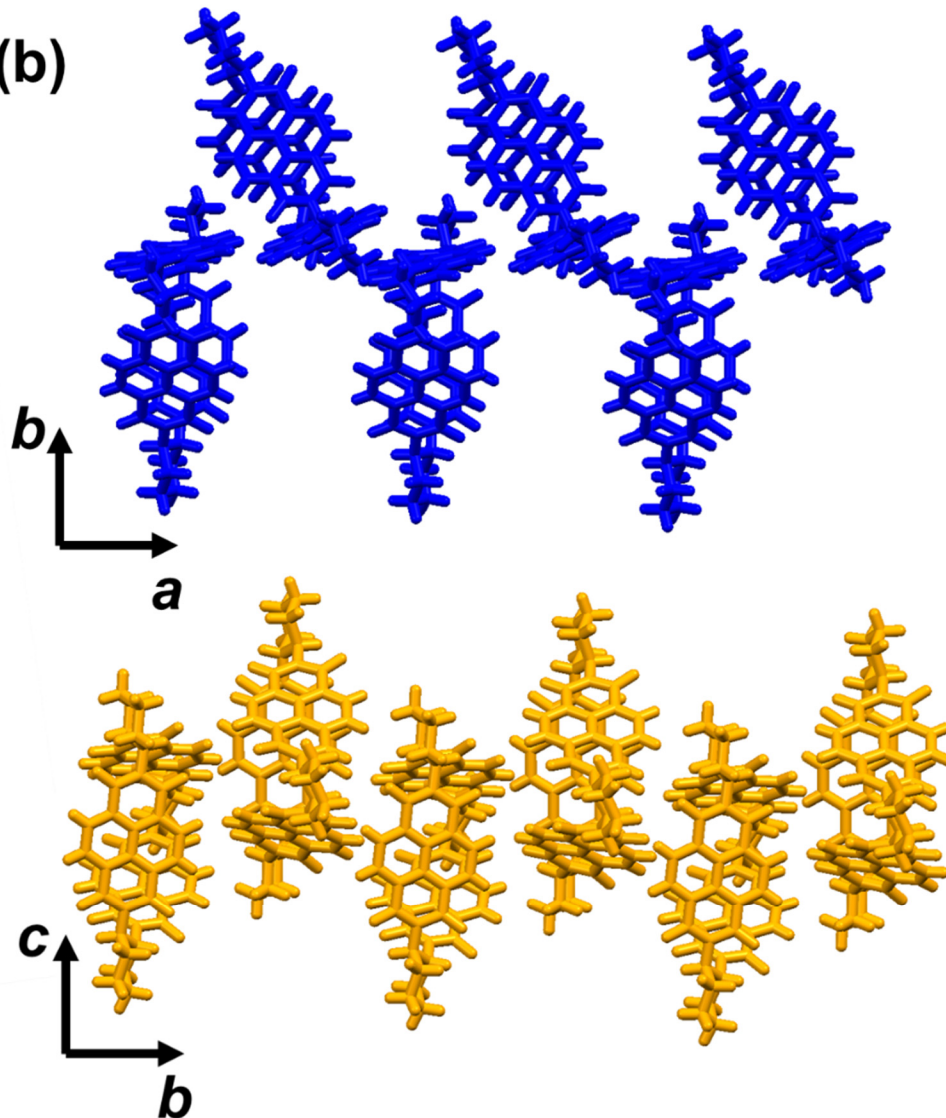


Figure 5

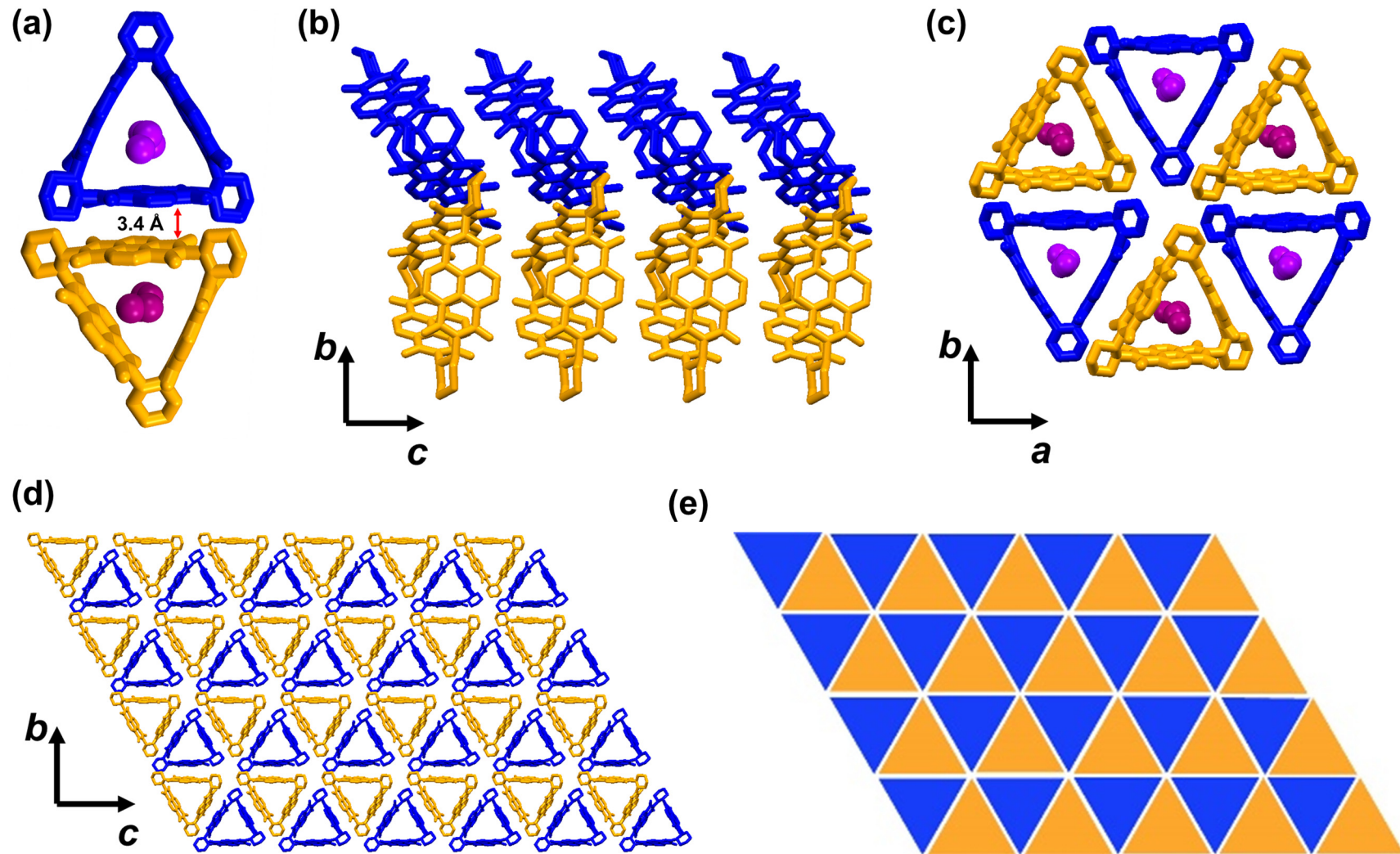


Figure 6

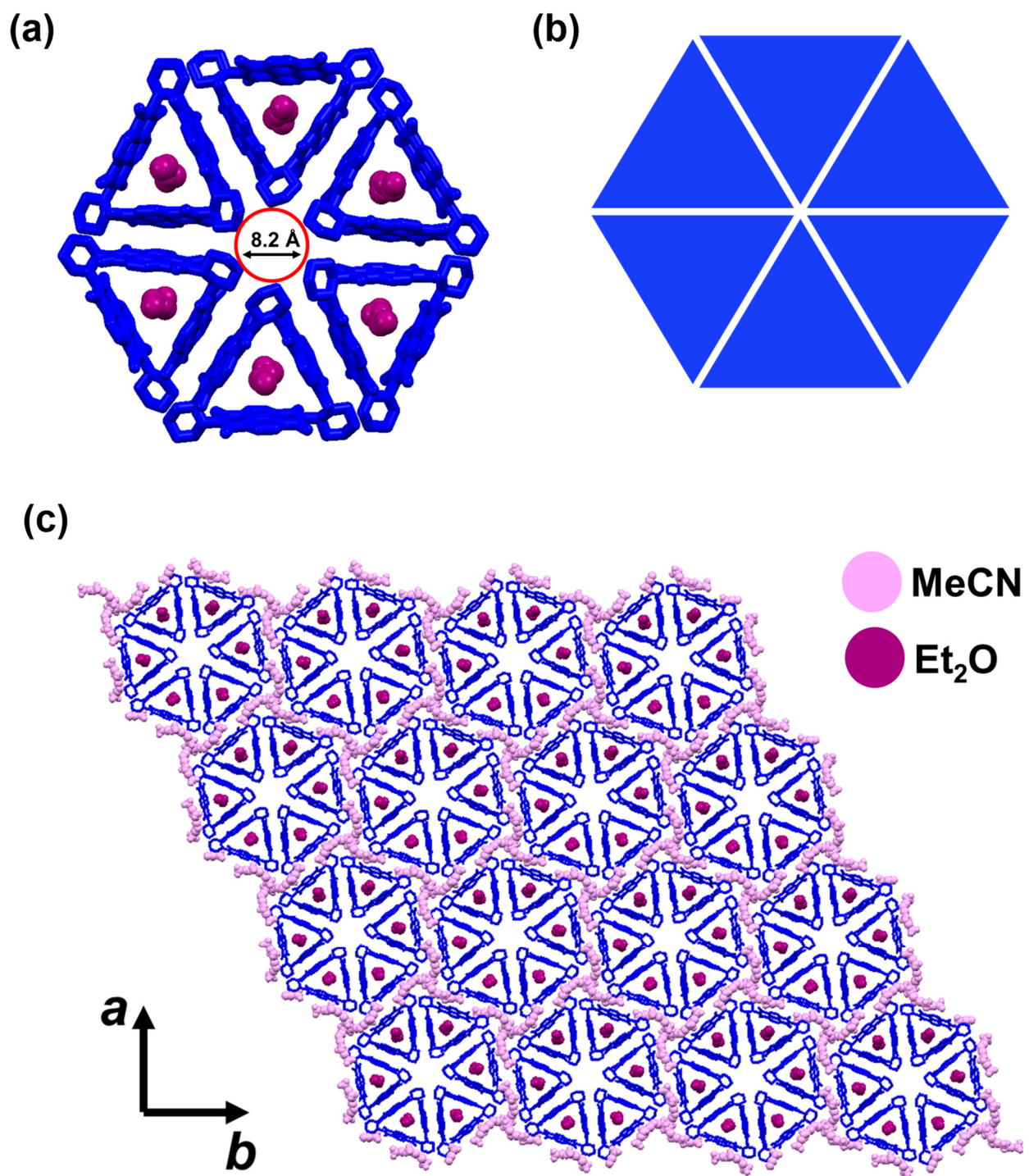


Figure 7

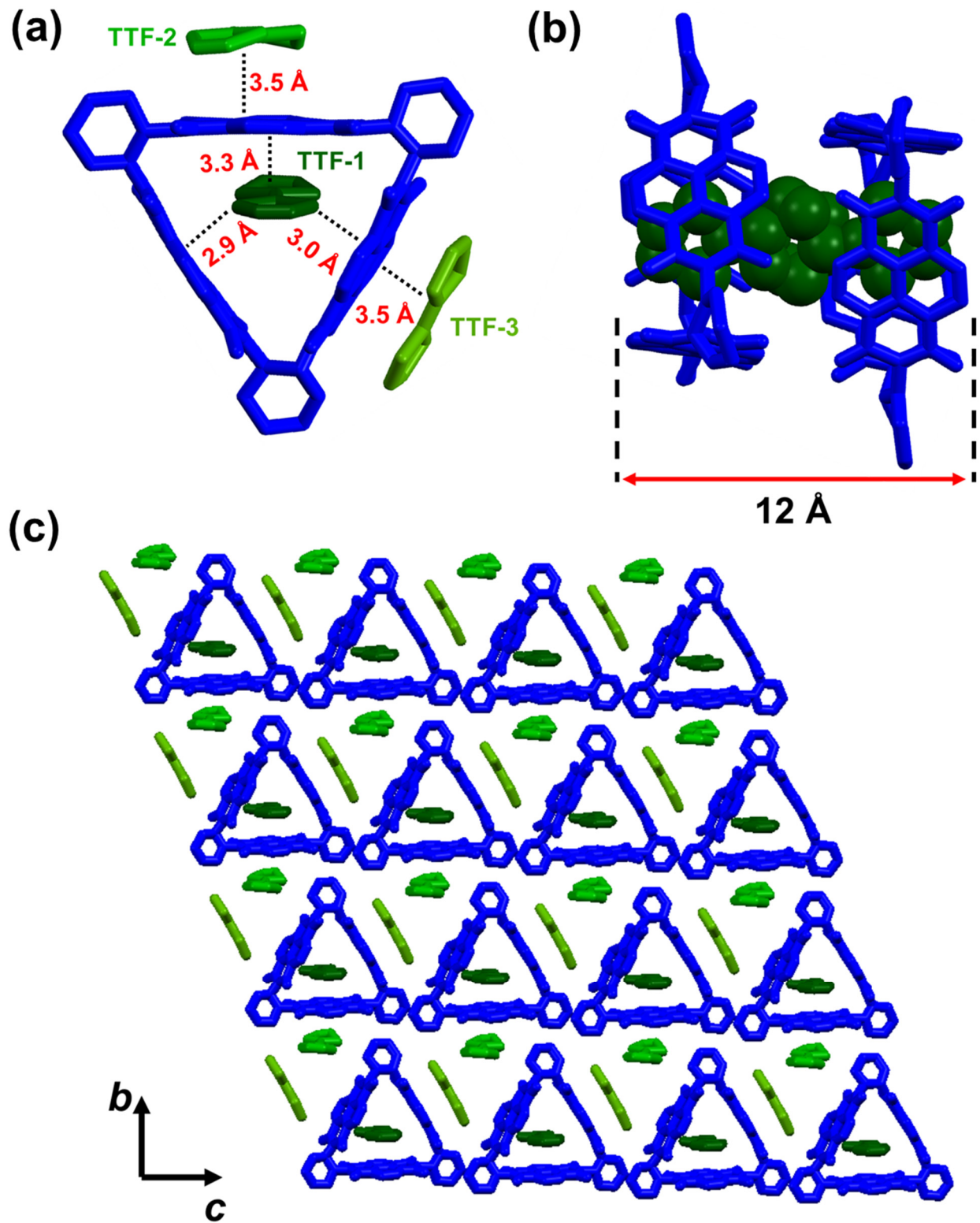
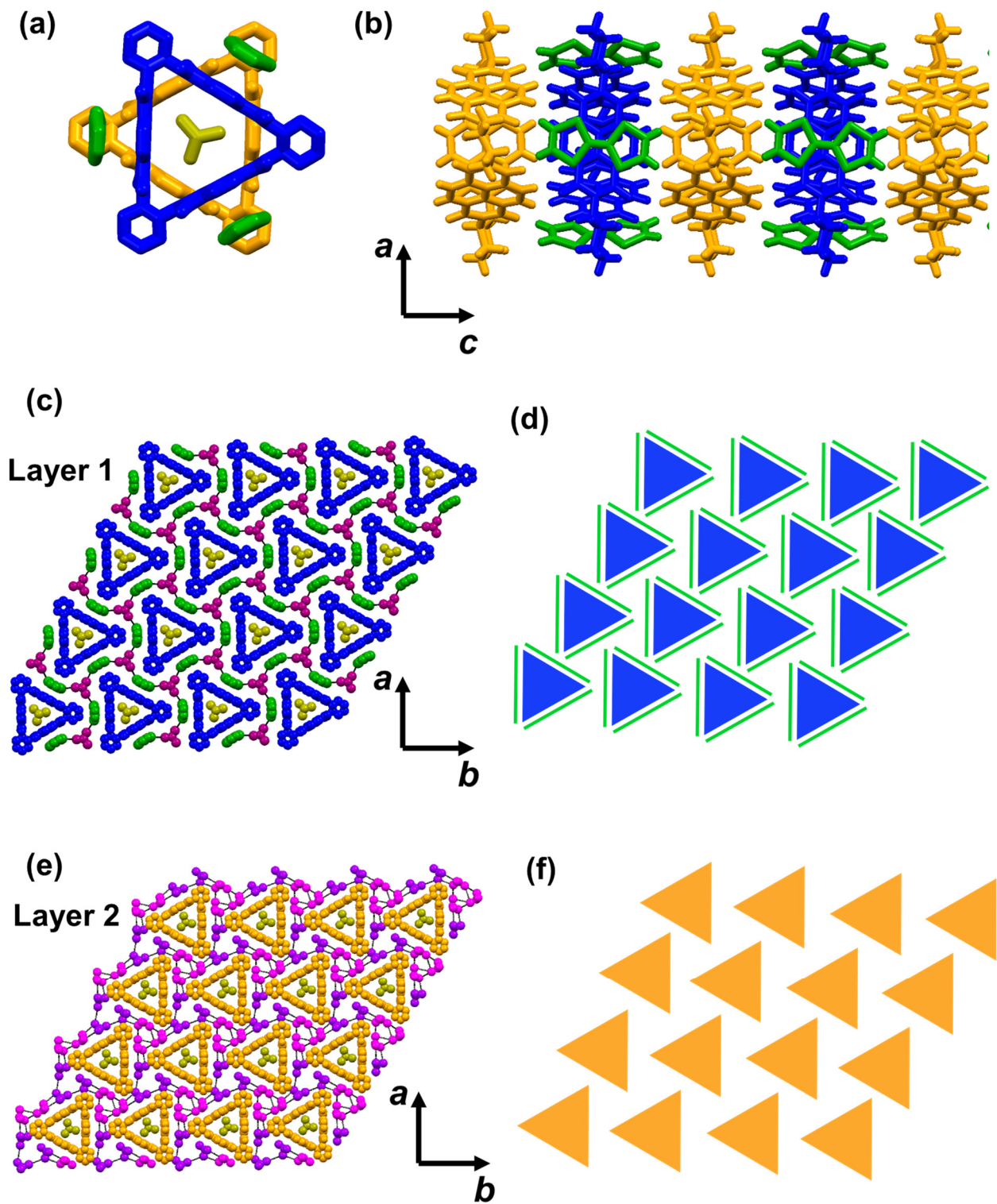


Figure 8



**Figure 9**

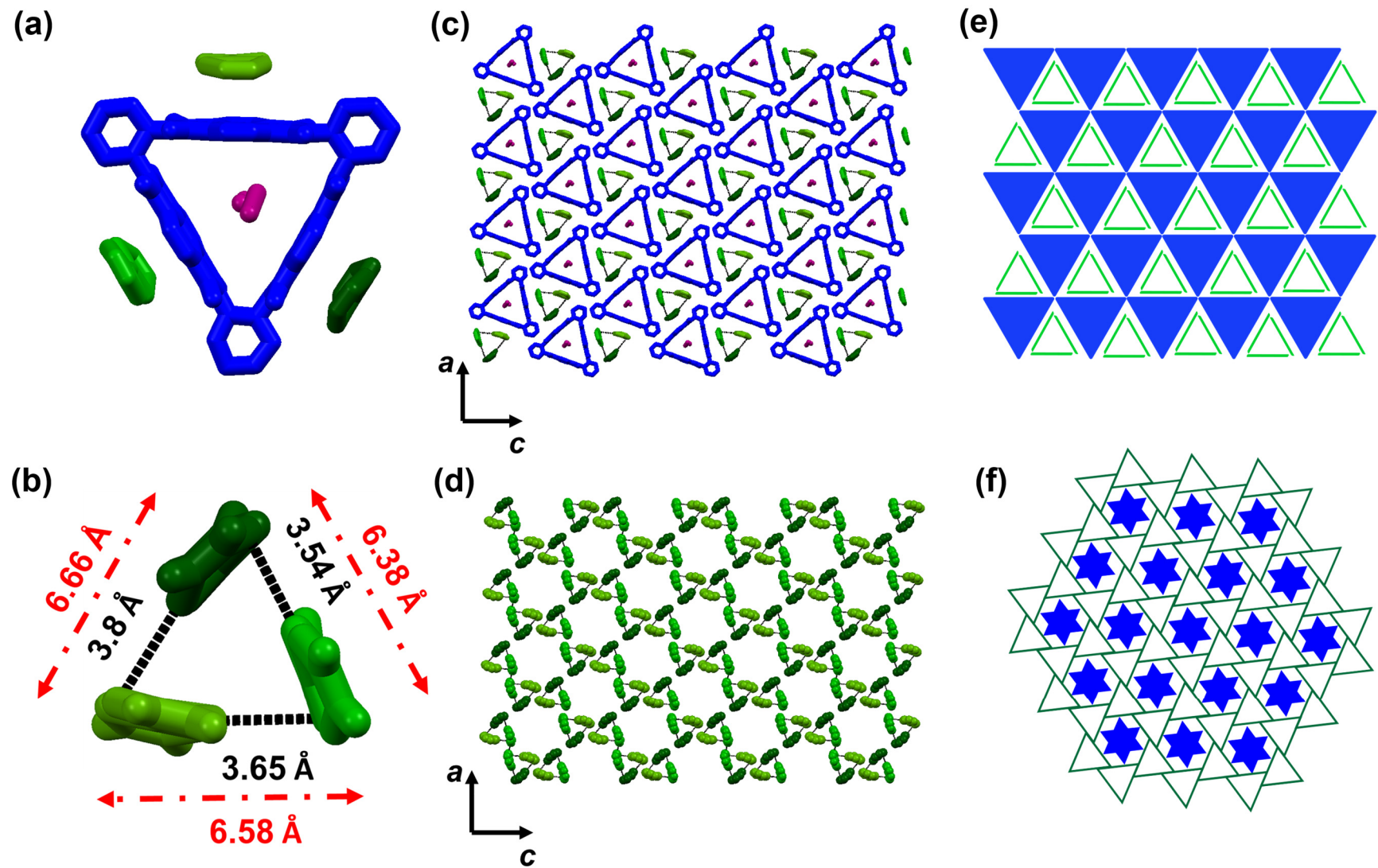


Figure 10

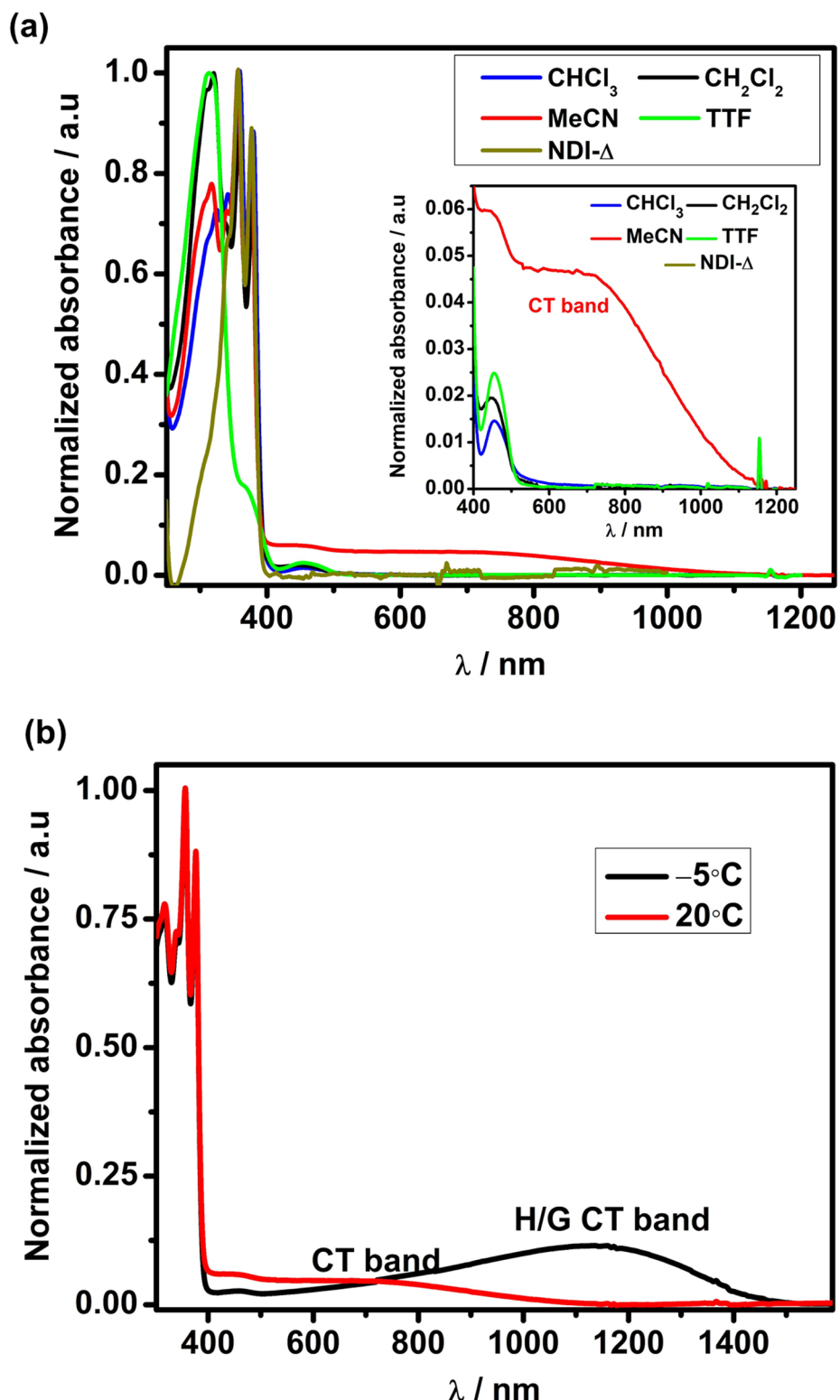


Figure 11

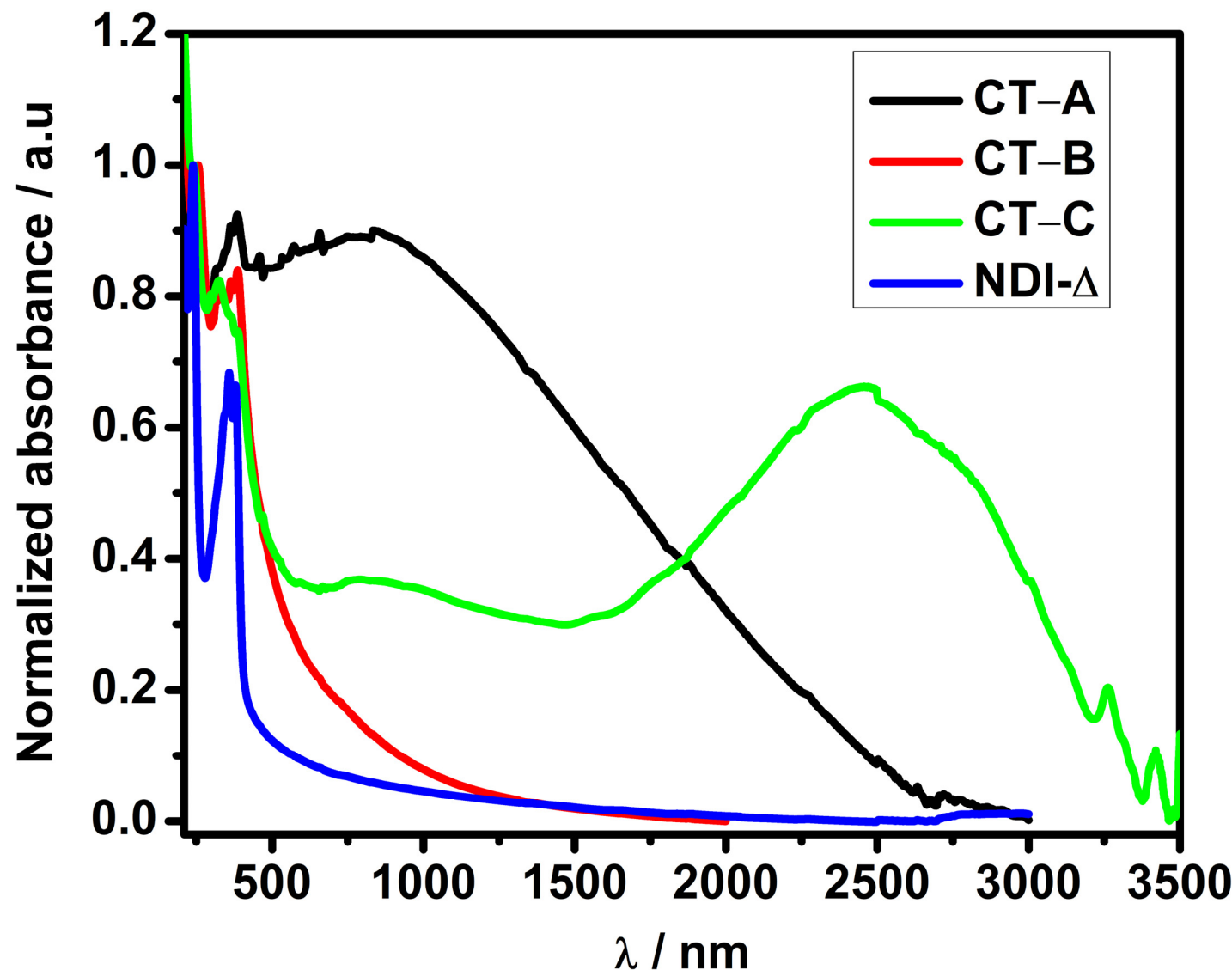
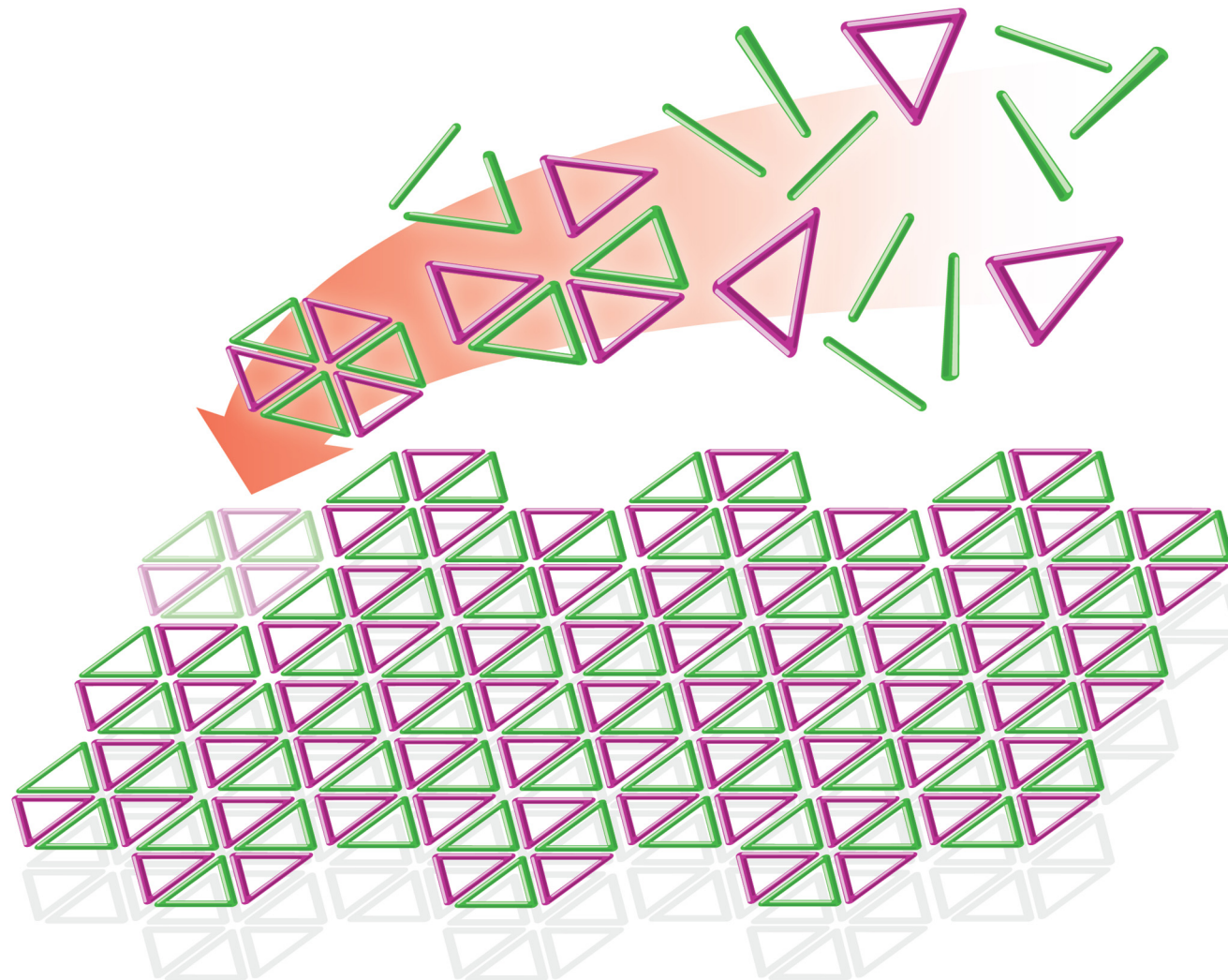


Figure 12



TOC

## Tables

**Table 1. Summary of Crystallographic Data for the Three Polymorphs of NDI-Δ Crystallized from MeCN/Et<sub>2</sub>O**

Parameters	α-NDI-Δ	β-NDI-Δ	γ-NDI-Δ
Formula	C <sub>60</sub> H <sub>42</sub> N <sub>6</sub> O <sub>12</sub> ·4(C <sub>2</sub> H <sub>3</sub> N)·0.5(C <sub>4</sub> H <sub>10</sub> O)	C <sub>60</sub> H <sub>42</sub> N <sub>6</sub> O <sub>12</sub> ·(C <sub>4</sub> H <sub>10</sub> O)	(C <sub>60</sub> H <sub>42</sub> N <sub>6</sub> O <sub>12</sub> )·(C <sub>4</sub> H <sub>10</sub> O)·(C <sub>2</sub> H <sub>3</sub> N)
FW	1039	1113.13	875.77
Temp. (K)	100(2)	100(2)	100(2)
Crystal system	Monoclinic	Triclinic	Hexagonal
Space group	<i>P</i> 2 <sub>1</sub>	<i>P</i> 1	<i>P</i> 6 <sub>2</sub>
<i>a</i> /Å	15.9512(11)	8.731(3)	34.8534(11)
<i>b</i> /Å	15.0324(11)	18.330(6)	34.8534(11)
<i>c</i> /Å	25.0891(17)	18.881(6)	8.5499(4)
<i>α</i> /°	90	62.204(7)	90
<i>β</i> /°	90.488(2)	85.045(8)	90
<i>γ</i> /°	90	77.442(7)	120
<i>V</i> /Å <sup>3</sup>	6015.8(7)	2608.7(4)	8830.8(7)
<i>Z</i>	4	2	8
<i>D<sub>c</sub></i> /mg.m <sup>-3</sup>	0.98	1.413	1.317
Unique reflns	34170	21111	9124
Reflns [ <i>I</i> >2σ( <i>I</i> )]	28363	7972	7558
<i>R<sub>int</sub></i>	0.041	0.181	0.055
<i>S</i>	1.02	0.97	1.03
<i>R<sub>1</sub></i> ( <i>I</i> > 2σ( <i>I</i> ))	0.056	0.098	0.069
<i>wR<sub>2</sub></i> (all)	0.149	0.224	0.195
Δρ <sub>max</sub> , Δρ <sub>min</sub> (e Å <sup>-3</sup> )	0.94, -0.94	0.34, -0.36	0.87, -0.41

**Table 2. Summary of Crystallographic Data for the NDI-Δ:TTF Cocrystals**

Parameters	CT-A	CT-B	CT-C
Formula	$C_{60}H_{42}N_6O_{12} \cdot 2.5(C_6H_4S_4) \cdot C_2H_3N$	$3(C_6H_4S_4) \cdot 4(CHCl_3) \cdot (C_{60}H_{42}N_6O_{12})$	$C_{60}H_{42}N_6O_{12} \cdot 3(C_6H_4S_4) \cdot CH_2Cl_2$
FW	1634.10	1150.21	3473.83
Temp. (K)	103(2)	100(2)	100(2)
Crystal system	Triclinic	Trigonal	Monoclinic
Space group	<i>P</i> -1	<i>P</i> 321	<i>P</i> 2 <sub>1</sub> /n
<i>a</i> /Å	15.8894(10)	19.1592(4)	18.1136(10)
<i>b</i> /Å	15.9601(10)	19.1592(4)	15.6480 (9)
<i>c</i> /Å	16.7929(12)	15.4941(4)	27.3059 (15)
$\alpha/^\circ$	69.422(4)	90	90
$\beta/^\circ$	69.338(4)	90	91.229
$\gamma/^\circ$	70.962(4)	90	90
<i>V</i> /Å <sup>3</sup>	3629.7(4)	4925.5(2)	7737.8(7)
<i>Z</i>	2	4	2
<i>D<sub>c</sub></i> /mg.m <sup>-3</sup>	1.495	1.552	1.491
Unique reflns	12346	8212	12665
Reflns [ <i>I</i> >2σ( <i>I</i> )]	11267	6646	11034
<i>R<sub>int</sub></i>	0.042	0.08	0.104
<i>S</i>	1.05	1.04	1.03
<i>R<sub>1</sub></i> ( <i>I</i> > 2 σ( <i>I</i> ))	0.114	0.094	0.196
<i>wR<sub>2</sub></i> (all)	0.318	0.270	0.379
Δρ <sub>max</sub> , Δρ <sub>min</sub> (e Å <sup>-3</sup> )	1.97, -0.72	1.09, -1.31	2.02, -1.09